

Department of Clinical Neuroscience, School of Medicine

Molecular MRI with hyperpolarized xenon and smart sensors

Ryan Patrick Hegarty, MPhys

Supervisors: Dr Henryk Faas, Dr Marie Christine Pardon,

Professor Thomas Meersmann

Contents

Introduction 4

1 Foundations of Magnetic Resonance

1.1 Classical description of NMR……. 7

1.2 Quantum Mechanical description of NMR……. 11

1.3 The net magnetization and predicting the energy of the system……. 13

1.4 Bloch Equations……. 15

1.5 The Signal……. 16

1.6 The FID……. 16

1.7 Fourier Transformation……. 18

1.8 Net magnetization and the signal……. 19

2 Investigating the metabolic response in the mouse brain after LPS administration using MR Spectroscopy

2.1 *In vivo* NMR spectroscopy background……. 20

2.2 Pulse Sequences……. 22

2.3 Echo Time……. 24

2.4 In vivo NMR spectroscopy in neuroinflammation……. 26

2.5 Introduction to study……. 31

2.6 Methods……. 33

2.7 Results……. 38

2.8 Discussion and Conclusion……. 40

3 Deuterium relaxation times in D_2O mixtures

3.1 Introduction……. 41

3.2 Methods……. 43

3.3 Results…… 45

3.4 Discussion and Conclusion……. 48

4 Targeted hyperpolarized ^{129}Xe biosensors

4.1 Introduction……. 49

4.2 ^{129}Xe Biosensors……. 50

4.3 ^{129}Xe MRI-background and current developments……. 52

4.4 Hyperpolarization of ^{129}Xe through spin exchange optical pumping……. 53

4.5 Chemical Exchange Saturation Transfer (CEST)……. 56

4.6 HyperCEST with ^{129}Xe……. 58

4.7 Xenon hosts……. 60

Concluding Remarks 61

References 63

Introduction

Research in biomedical imaging brings together physicists, chemists, biologists and engineers all with a shared interest in the development of imaging methodologies for examining biological structure and function. It is a large field encompassing work in techniques such as x-ray imaging, computed tomography (CT) imaging, optical imaging, nuclear medicine, and magnetic resonance imaging (MRI) and spectroscopy (MRS). These techniques can derive information from biomedical images that range in scale from human imaging to mouse imaging down to molecular/cellular imaging.

Imaging in biomedical research has become increasingly important especially in drug development and it is an important facet of preclinical and translational research in biology. For example, imaging animal models that are predictive of the human response to a particular pathology has enabled drug developers to access real time data on a drug's bio distribution, efficacy and kinetics at all stages of disease and has had a dramatic impact on drug discovery and development. Preclinical imaging is a powerful and clinically translatable tool for monitoring disease progression.

Imaging tools enable us to make a better assessment of anatomy, physiological and functional parameters along with molecular and cellular processes. They cover a broad spectrum and have important applications in areas such as cancer research, neuroimaging, cardiac imaging, stroke models and inflammation.

One area of imaging that has found itself having an emerging role in the development of medical devices and drugs is that of imaging biomarkers. A biomarker [1] may be defined as any biological parameter, and it could be genetic, biochemical, metabolic, histologic, anatomic, physical or functional. Imaging of biomarkers is the detection of any of these parameters through imaging to help detect or monitor disease. Imaging biomarkers can be classified in several different ways; diagnostic/prognostic biomarkers are used to predict a patient's clinical outcome, monitoring biomarkers predict a patient's clinical outcome after administration of a drug (e.g. FDG PET monitoring for tumour recurrence after

cancer treatment/therapy), and response biomarkers used in drug trials to see if a particular drug will change the clinical outcome in a group of patients/volunteers.

MRI has high spatial resolution but inherently low signal. Because the NMR properties of nuclei such as hydrogen (or protons) in water are affected by a variety of physiological parameters, MRI can be used to image a wide range of tissue properties including cellular density [2], iron content [3], oxygenation[4], water content[5], and metabolite concentration[6].

MRI probes such as gadolinium, iron oxide or ^{19}F containing molecules can be used to investigate changes more specifically. These probes can improve sensitivity, and provide unique biomarkers for properties such as tissue perfusion, blood flow and blood volume. Despite its relatively low sensitivity compared to other imaging modalities, MRI is still one of the most widely used tools in clinical radiology and a popular research tool in clinical and preclinical applications.

The main aim of this project was to develop an understanding of both the theoretical and experimental aspects of MRI and NMR spectroscopy, while also gaining expertise in hyperpolarized xenon MRI methods.

The first chapter will introduce the basics of NMR required to understand the work presented in subsequent chapters. Chapter 2 explores the area of spectroscopic biomarkers for certain pathologies, including those linked to neuroinflammation and a pilot study was performed examining the effect of induced neuroinflammation on metabolite levels in the mouse brain. Neuroinflammation plays a key role in a wide range of brain disorders including chronic pain, stroke, Parkinson's and Alzheimer's disease.

The purpose of this pilot study was to investigate how the concentration levels of certain metabolites believed to be biomarkers of neuroinflammation (in particular myo-inositol) can be monitored non-invasively using MR spectroscopy and thus assist in validating them as biomarkers for neuroinflammation. This gives us specificity, one of the key aims for molecular imaging. Ultimately this may lead to an

increased understanding of the disease mechanisms and assist in monitoring disease progression.

Chapter 3 contains results from a D_2O relaxometry study. Through this work a greater understanding of the fundamentals of NMR relaxation measurements was gained. It also lead to an increased understanding the role of contrast agents for MRI. Contrast agents can improve the relative difference in signal intensity between two adjoining tissues. This is important as sometimes distinction between a region of interest and its surrounding environment is impossible due to tissue properties being too similar or cancellation of signals by space averaging.

Chapter 4 contains an overview of current developments in hyperpolarized xenon biosensors. MRI suffers from an inherent lack of sensitivity compared to other imaging modalities, something which can be overcome in hyperpolarization via optical pumping. The concept of a hyperpolarized xenon biosensor along with some relevant background theory will be presented here.

Finally, conclusions on the research conducted will be presented along with a description of a future project being carried out which is of great interest due to its relevance to work presented here.

1 Foundations of Magnetic Resonance

Nuclear magnetic resonance (NMR) is the study of the magnetic properties of the nuclei, which had been independently discovered by Bloch and Purcell in 1946. They described a method of measuring the spin angular momentum of the nucleus and it interaction with an external magnetic field and for this they shared the Nobel Prize for Physics in 1952. The purpose of this chapter is to provide the background physics necessary to understanding the work presented in subsequent chapters. In particular, the origin of the NMR signal and the nature of magnetization will be described. NMR is a well-developed field with an abundance of quality resources giving a thorough description of the topic; 3 particularly useful references were consulted for the theory presented in this chapter[7-9].

1.1 Classical description of NMR

The whole of NMR is based on nuclear spin, in order to simplify the visualization of spin angular momentum it is worth describing some relations from classical matters before going into the quantum mechanical description.

Motion whether rotational or linear, will always have a corresponding momentum. This can be linear or angular momentum. For example, an object of mass m and velocity **v** will have a linear momentum **p** equal to

$$\vec{p} = m\vec{v} \quad (1.1)$$

The linear momentum of an object will only change if a force **F** is applied, this is given by Newton's second law:

$$\vec{F} = \left(\frac{d\vec{p}}{dt}\right) = m\vec{a} \quad (1.2)$$

Where **a** is equal to the acceleration of the object i.e. the rate at which the object changes its velocity and is measured in m/s^2. Without the presence of an external force, the object would maintain constant momentum and speed. Now consider an object that has constant velocity and is rotating about a fixed point at a distance **r**. This object will have angular momentum **L** measured in kilogram metres squared per second ($kg\text{-}m^2/s$), given by:

$$\vec{L} = \vec{r} \times \vec{p} \quad (1.3)$$

So, its magnitude will be m**vr** and its direction perpendicular to the plane of motion. The angular momentum of an object can only be changed if an external torque is applied (similar to the linear momentum description). Torque is given by the cross product of the distance over which the force has to be delivered and is measured in N·m:

$$\vec{T} = \vec{r} \times \vec{F} = \vec{r} \times \left(\frac{d\vec{p}}{dt}\right) = \frac{d\vec{L}}{dt} \quad (1.4)$$

Consider now a situation in which this rotating object is carrying an electric charge thus creating a current loop. In accordance with classical physics this current will generate a magnetic field with a magnetic dipole moment μ equal to the current times the area and measured in Newton-metres per Tesla (N.m/T). If an object with mass m and charge e rotating with a velocity v about a fixed point at a distance **r**, **μ** is equal to:

$$\vec{\mu} = \left[\frac{e\vec{v}}{2\pi\vec{r}}\right]\pi\vec{r}^2 \quad (1.5)$$

If we use the relation **L**=m**vr**, we find that:

$$\vec{\mu} = \left(\frac{e}{2m}\right)\vec{L} = \gamma\vec{L} \quad (1.6)$$

Where γ is the gyromagnetic ratio. This relationship is valid for any orbital, or periodic motion and is specific for different nuclei [10].

Isotope	Spin	Gyromagnetic ratio ($\gamma/10^7$ rad $s^{-1}T^{-1}$)	Natural Abundance x/%
^{1}H	1/2	26.7522128	99.9885
^{2}H	1	4.10662791	0.0115
^{13}C	1/2	6.728274	1.07
^{19}F	1/2	25.18148	100
^{129}Xe	1/2	0.6192895	26.44

Table 1.1 Gyromagnetic ratio of selected nuclei

Then the rotating object described previously is placed in an external magnetic field $\mathbf{B_0}$, the current loop will experience a torque equal to:

$$\vec{T} = \vec{\mu} \times \vec{B}_0 \quad (1.7)$$

Combining with (1.4), (1.6) and (1.7) gives:

$$\left(\frac{d\vec{\mu}}{dt}\right) = \gamma\vec{\mu} \times \vec{B}_0 \quad (1.8)$$

Since magnetic dipole moment remains constant, the differential equation above describes how $\boldsymbol{\mu}$ rotates (precesses about $\mathbf{B_0}$). It can also be described by:

$$\left(\frac{d\vec{\mu}}{dt}\right) = \vec{\mu} \times \vec{\omega}_0 \quad (1.9)$$

Combining (1.8) and (1.9) describing the precession of **μ** around $\mathbf{B_0}$ gives:

$$\vec{\omega}_0 = \gamma \vec{B}_0 \quad (1.10)$$

This is the famous Larmor equation, which underpins the whole of NMR. The precession or Larmor frequency ($\boldsymbol{\omega_0}$) refers to the rate of precession of the magnetic moment of a given nuclei around the external magnetic field, and is directly proportional to the gyromagnetic ratio and the applied magnetic field.

The magnetic moment described above, will also have an associated magnetic energy given by:

$$E = -\vec{\mu} \cdot \vec{B}_0 = -\mu B_0 cos\theta \quad (1.11)$$

Where θ is the angle between the external magnetic field $\mathbf{B_0}$ and the magnetic moment. According to this equation the magnetic energy would be at a minimum when **μ** is parallel to $\mathbf{B_0}$ (θ=0˚) and its maximum value when **μ** is antiparallel to $\mathbf{B_0}$ (θ=180˚).

1.2 Quantum Mechanical description of NMR

One fundamental aspect of quantum mechanics is that the angular momentum of protons, electrons, and neutrons is restricted to certain values, i.e. it is quantised and the angular momentum **L** is given by:

$$\vec{L} = \left(\frac{h}{2\pi}\right)\sqrt{\vec{I}(\vec{I}+1)} \quad (1.12)$$

Where h is Planck's constant (expressed in J·s) and **I** is the spin quantum number which can only have half integer or integer values. Since it is a vector, it also has a directional component associated with it and the quantum mechanical direction of angular momentum is given by the quantum number m. For example, angular momentum in the z direction is given by:

$$L_z = \left(\frac{h}{2\pi}\right)m \quad (1.13)$$

Quantum mechanics tells us that m can have 2I+1 values

$$m = I, I-1, I-2, \ldots, -I \quad (1.14)$$

For protons, electrons and neutrons, I equals ½. For different nuclei, I can be deduced using the charge number and the atomic mass along with these rules:

1. For nuclei with an even mass number and even charge number, I is zero eg. ^{12}C (I=0), ^{16}O (I=0)
2. For nuclei with an odd mass number, I is half-integral eg. ^{1}H (I=1/2), ^{13}C (I=1/2)
3. For nuclei with an odd charge number and even mass number, I is an integral number eg. ^{2}H (I=1), ^{14}N(I=1)

Nuclei have a magnetic moment **μ** which is related to the angular momentum **L** by:

$$\vec{\mu} = \gamma\vec{L} \quad (1.15)$$

Where γ as described before, so because the angular momentum is quantised, the magnetic moment will also be quantised and using eq(1.13) its magnetic moment along z can be given by:

$$\mu_z = \gamma \left(\frac{h}{2\pi}\right) m \quad (1.16)$$

From the classical description of NMR we know that a magnetic moment in an external magnetic field has an associated magnetic energy given by:

$$E = -\vec{\mu} \cdot \vec{B}_0 \quad (1.17)$$

By combining (1.16) and (1.17) we find that

$$E = \vec{\mu} \cdot \vec{B}_0 = -\gamma \left(\frac{h}{2\pi}\right) m\vec{B}_0 \quad (1.18)$$

Since m is quantised, the energy levels are also quantised. For example, a particle with spin I=1/2 has two energy levels (m=+1/2, m=-1/2) and has an energy difference given by:

$$\Delta E = \gamma \left(\frac{h}{2\pi}\right) B_0 \quad (1.19)$$

The resonance in NMR is achieved through the application of an RF pulse perpendicular to μ_z with frequency ν_0, with an energy equal to that given in eq(1.19) this can be written as

$$\Delta E = h\nu_0 \quad (1.20)$$

Combining (1.19) and (1.20) gives the previously described Larmor equation:

$$\nu_0 = \left(\frac{\gamma}{2\pi}\right) B_0 \quad (1.21)$$

1.3 The net magnetization and predicting the energy of the system

When a group of spins are placed in a magnetic field, each individual spin can align in one of two possible ways. The spin can align with the magnetic field (low energy) or against the magnetic field (high energy). At room temperature there are more spins in the lower energy level than in the higher energy level. The energy difference between both states is proportional to the magnitude of B_0:

$$\Delta E = \gamma \hbar B_0 \quad (1.22)$$

There is a difference in spin population between the two states due to the presence of an external magnetic field. If we let N↑ represent the number of spins in the lower energy state and N↓ represent the number of spins in the higher energy state, the population difference can be found using the Boltzmann distribution

$$\frac{N\uparrow}{N\downarrow} = \exp\left(\frac{\Delta E}{k_B T_s}\right) \quad (1.23)$$

Where k_B is Boltzmann's constant and T_s is the spin temperature. This small population difference can be increased using a higher magnetic field or lowering the temperature. This is important to bear in mind as the signal in NMR is a direct result of the energy absorbed by the spins which move from N↑ to N↓ and the energy emitted by spins which go from N↓ to N↑.

This population difference (N_s) induces the net magnetization called M_0

$$M_0 = \frac{\gamma^2 \hbar^2 B_0 N_s}{4 k_B T_s} \quad (1.24)$$

When considering bulk magnetization **M**, which is all of the magnetic moments in a sample. When placed in a magnetic field, the bulk magnetization will experience a torque

$$\frac{d\vec{J}(t)}{dt} = \vec{M}(t) \times \vec{B}(t) \quad (1.25)$$

J is the bulk spin angular momentum, and along with **M** and **B** is time dependent due to the application of RF pulses on the x and y axis.

Using $\mu_z = \gamma I_z = \gamma \hbar m$ and the equation above, we find that

$$\frac{d\vec{M}(t)}{dt} = \vec{M}(t) \times \gamma \vec{B}(t) \quad (1.26)$$

which is the basis of the Bloch equations.

This states that if the magnetization is pushed out of alignment with **B**, it will precess around **B**. This classical approach is generally used to describe the evolution of magnetism as it is the most intuitive way to explain macroscopic observations made in MRI.

1.4 Bloch Equations

The magnetization $\vec{M}$, which is proportional to the signal in a NMR experiment and is the sum of the individual magnetic moments in a sample is given by

$$\vec{M} = \sum_{i=1}^{N} \vec{\mu}_i \quad (1.27)$$

Assuming the magnetization is initially pointing in the z-axis, the introduction of a static magnetic field $\overrightarrow{B_0}$ and an oscillating magnetic field $\overrightarrow{B_1}$ will affect the direction and magnitude of $\vec{M}$. If $\frac{d\vec{M}}{dt} = \gamma(\vec{M} \times \vec{B}(t))$ then the complete equations of motion for spin magnetization, the Bloch equations are:

$$M_x = \gamma\left(M_y B_z - M_z B_y\right) - \frac{M_x}{T_2} \quad (1.28)$$

$$M_y = \gamma(M_z B_x - M_x B_z) - \frac{M_y}{T_2} \quad (1.29)$$

$$M_z = \gamma\left(M_x B_y - M_y B_x\right) - \frac{M_z - M_0}{T_1} \quad (1.30)$$

Where T_1 and T_2 are the longitudinal and transverse decay constants respectively, they will be described in detail later in this report. It is important to understand these equations both in the laboratory and rotating frame as they describe the time dependence of the net magnetization during the course of the NMR experiment. These equations are known as the Bloch equations and give insights into many processes in NMR, and will be discussed further later in this report.

1.5 The Signal

The signal recorded in an NMR experiment can come from a range of nuclei including ^{1}H, ^{31}P,^{2}H, ^{13}C, ^{19}F, and ^{129}Xe. An RF pulse is used to excite spins in a sample which in turn gives us a signal dependent on the NMR properties and position of each spin. This is the basis of the simplest NMR experiment which is to perturb the magnetic moment from the magnetic moment from the longitudinal plane to the transverse plane using a RF pulse at the Larmor frequency. Once the RF pulse is switched off, a voltage is detected on the receiver coil via Faraday induction. An oscillating signal at the resonant frequency that follows an exponential decay can then be observed. This is called an FID (Free Induction Decay), and its rate of decay depends on the T_2* of the sample. This FID gives information about the environment of the spins and is at the base of all NMR experiments.

1.6 The FID

The simplest NMR experiment is to perturb the magnetic moment from the longitudinal plane into the transverse plane using a short radiofrequency pulse B_1, and then observe the signal in the receiver coil. One can observe the following: an oscillating signal that follows an exponential decay. Shown below in Figure 1.2.

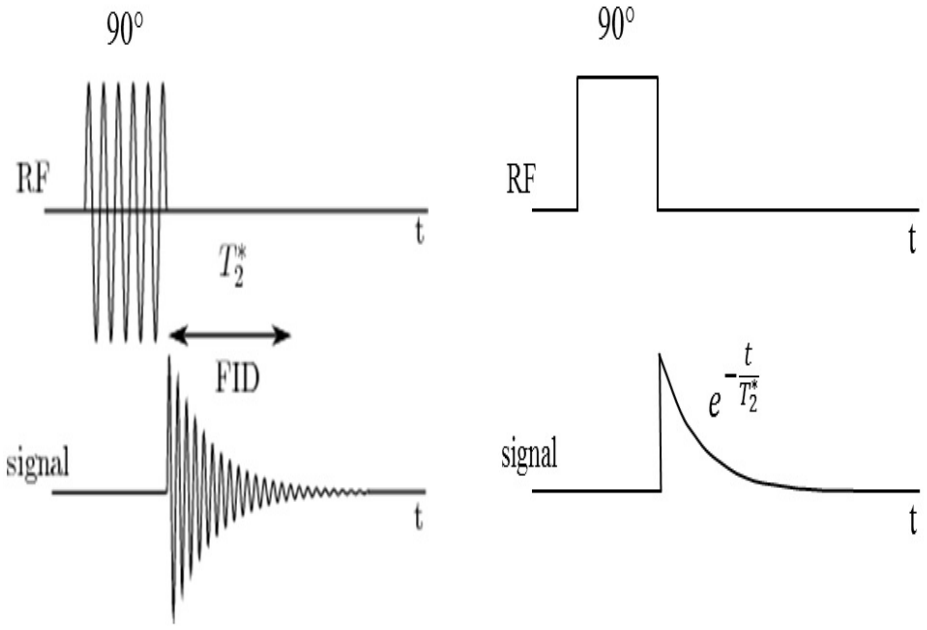


Figure 1.2 Sequence diagram of a free induction decay (FID) experiment. Left: RF pulse and signal in the laboratory frame of reference. Right: RF pulse and signal in the rotating frame.

This can be visualised by thinking of the net magnetization as a vector being tipped away from the z-axis by the application of B_1. Note that signal is only detected when a vector exists in the transverse plane. Maximum signal is achieved when the net magnetization is tipped by 90˚. It is worth remembering that a time delay must be included in an FID experiment to allow the magnetization in the z-direction to be re-established.

1.7 Fourier Transformation

The Fourier transform is a mathematical technique for converting time domain data to frequency domain data, and vice versa. A signal at one point in time will have a corresponding Fourier transform with one peak at that same frequency. If the signal is made up of several oscillations, the signal will have multiple peaks at different frequencies, and the Fourier transform is a mathematical representation of that spectrum.

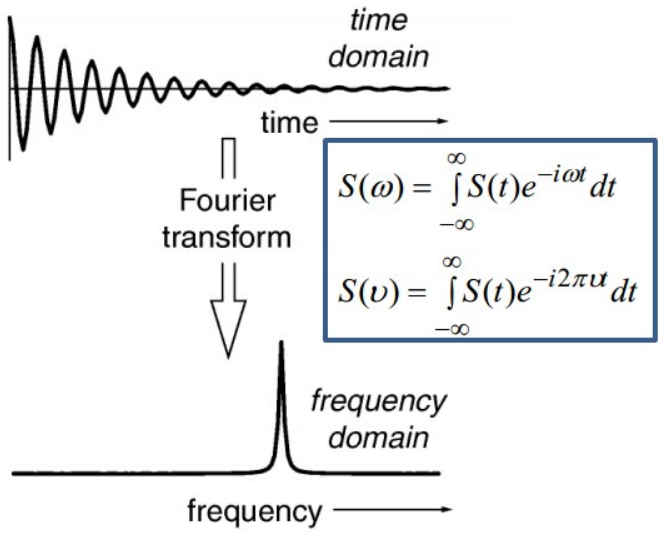


Figure 1.3 Fourier Transform

It is important to remember that in a spectrometer the FID is not detected as a continuous signal (which figure 1.3 represents) but as a sum of a discrete set of N digital points at different times and then the spectrum is computed, this is called FFT (Fast Fourier Transform).

1.8 Total Magnetisation and the Signal

Let us recall the expression for the net magnetization:

$$M_0 = \frac{\gamma^2 \hbar^2 B_0 N_s}{4 k_B T_s}$$

The net magnetization described above is an important quantity when considering the available signal for MR experiments, and from this we can see the relatively few parameters which affect M_0. The net magnetization has a square dependence on the gyromagnetic ratio of nuclei, showing the benefit of using nuclei such as hydrogen which have a high gyromagnetic ratio (see Figure 1.1). The net magnetization has a linear dependence on the field, illustrating the benefit of performing MR experiments at a higher magnetic field. The number of nuclear spins N_s is another important parameter relating to the net magnetisation and therefore the signal intensity. It comes from the difference in population between the two spin states, and can be increased dramatically to overcome the limited signal arising from the small population difference. One such method to achieve this is hyperpolarization through spin exchange optical pumping which will be explored in Chapter 4.

2 Magnetic Resonance Spectroscopy Methods

In the following sections some background detail on *in vivo* NMR Spectroscopy will be given, including elements such as commonly used pulse sequences, the effect of echo times, and why *in vivo* NMR spectroscopy and the role it can play in neuroinflammation studies.

2.1 *In vivo* NMR Spectroscopy Background

In vivo NMR spectroscopy of the brain can reveal a wealth of metabolic information since it can measure the levels of metabolites. For example, in a mouse brain the levels of 17 metabolites can be detected using proton NMR spectroscopy which can be used in metabolic research or as biomarkers in diagnosing certain pathologies. It has the capabilities to show this information not only from a single localized region (single voxel) but also as a spatial map of the entire brain using multiple localization or magnetic resonance spectroscopic imaging (MRSI). Single voxel spectroscopy has the advantages of the volume being well defined, magnetic field homogeneity can be readily optimised and improved water suppression and spectral resolution. However, it has the disadvantage that no signal is obtained from large parts of a subject therefore potentially missing important information. MRSI can be used to overcome this problem. It allows for the detection of localized NMR spectra from an array of directions. However, it is technically more challenging due to magnetic field inhomogeneities across a sample, spectral degradation due to inter-voxel contamination and long data acquisition times.

Mice are often the focus of many *in vivo* NMR spectroscopy studies due to the many transgenic models available to investigate metabolism or mimic common diseases found in humans [11].

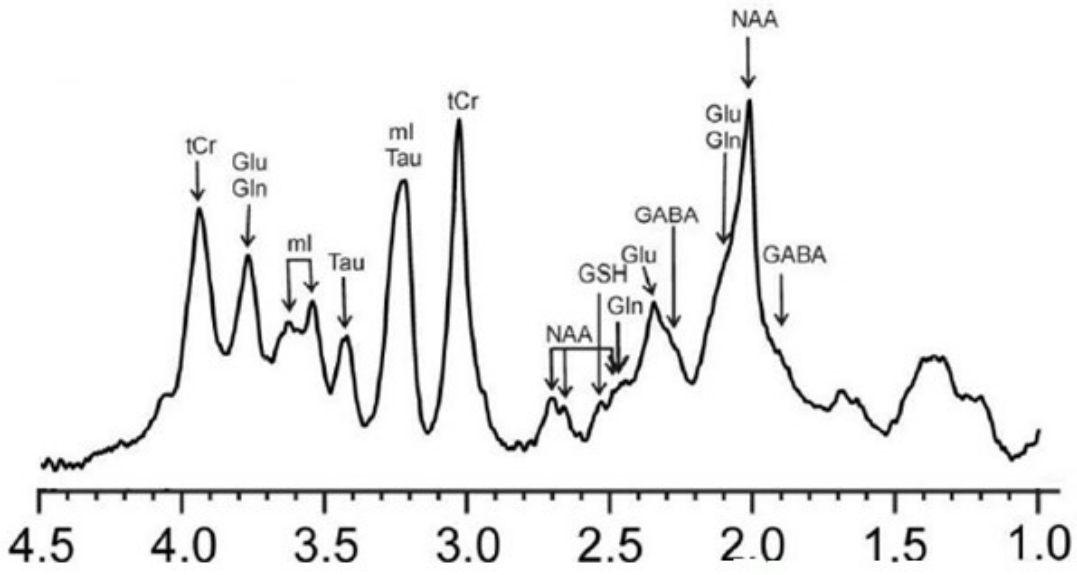


Figure 2.1 Sample NMR spectrum from mouse brain taken at 9.4T from Braakman et al. [12]

In mice, both spatial mapping of metabolites and spectra from single voxels can be achieved, however most published work in this area is single voxel. This is partly due to the superior quality of spectra one can achieve in a single voxel, and also the technical difficulties in spatial mapping of metabolites over the whole brain.

NMR spectroscopy data of good quality must meet a few prerequisites:

1. The SNR must be sufficient to detect changes in metabolites with respect to controls.
2. The signals from the water content must be suppressed to limit contamination of the spectra.
3. A good B_0 shim must be obtained so that the metabolites can be distinguished. A good shim will reduce signal overlap by minimizing the linewidths of the peaks.
4. Signals from outside the volume of interest must also be suppressed.

5. There must be good spatial resolution in the anatomical image taken prior to doing spectroscopy so we know exactly where to place our voxel in the anatomical area we are interested in.

2.2 Pulse Sequences

The following pulse sequences are the most common pulse sequences used in single voxel MR spectroscopy. A brief description of each pulse sequence will be given along with an overview of their advantages and disadvantages.

PRESS (Point Resolved Spectroscopy)(Figure 2.2) uses one 90˚ pulse and two 180˚ refocusing pulses to create a spin echo while STEAM (Stimulated Echo Acquisition Mode)(Figure 2.3) uses three 90˚ pulses to create a stimulated echo. The main difference between the two, being that PRESS has twice the signal compared to STEAM, due to half of the signal in STEAM being lost by creation of a stimulated echo. It is for this reason that PRESS is more commonly used. However, STEAM has some advantages over PRESS. For example, STEAM requires lower RF power (lower SAR) because it uses only 90˚ pulses. PRESS uses more RF power (higher SAR) as it uses two 180˚ pulses. STEAM can also achieve shorter echo times which is useful for the detection of metabolites with short T_2 values such as glutamate (Glu), glutamine (Glu), myo-Inositol (mI). STEAM can achieve these short echo times because transverse relaxation does not occur between the second and third 90˚ pulses and also due to the fact that 90˚ pulses are shorter than 180˚ pulses, which STEAM requires.

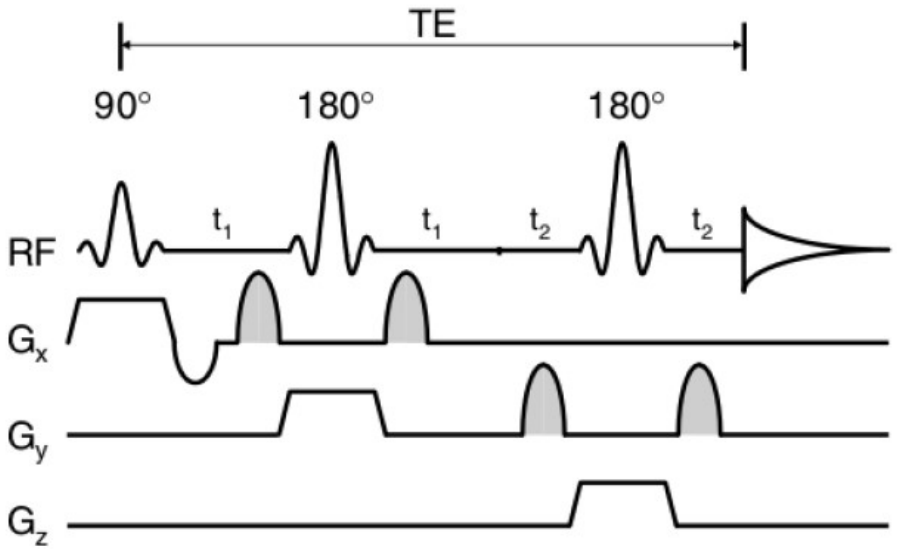


Figure 2.2 PRESS sequence which uses a 90˚ excitation pulse followed by two 180˚ slice-selective refocusing pulses

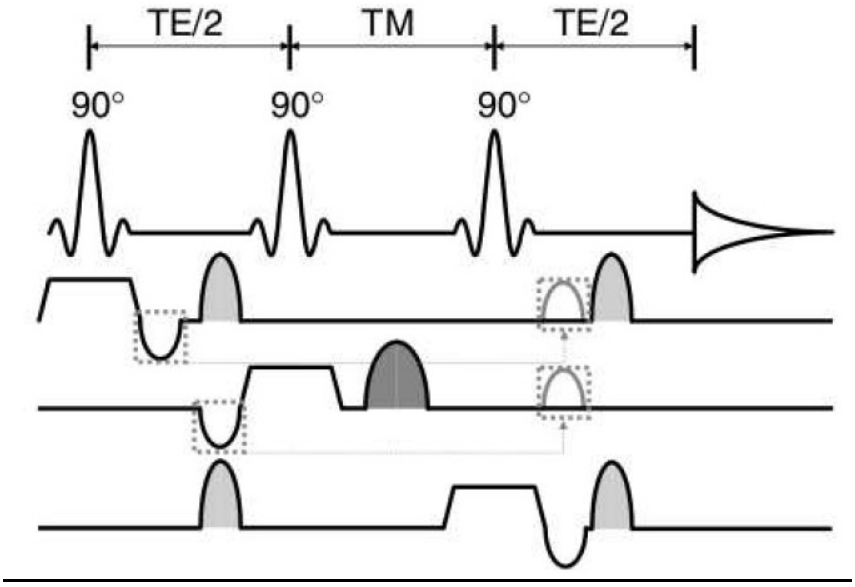


Figure 2.3 STEAM sequence which consists of three 90˚ slice-selective pulses

Both sequences are highly effective localization methods, and volume selection in both is based on similar principles. In addition to offering a factor of two gain in signal, PRESS also has the advantages of being less sensitive to motion and diffusion, and is insensitive to multiple-quantum effects. Both sequences have their merits and drawbacks, which are worth considering when designing your experiment.

2.3 Echo Time

The most important acquisition parameter in a MR spectroscopy sequence is the echo time (TE). In fact, one could separate MR spectroscopy into short TE and long TE methods. TE is the time the magnetization is in the transverse plane after an excitation and before the signal readout. During this time TE, the signal from each metabolite peak relaxes with its own T_2 relaxation time.

Choosing long echo times simplify spectra, because the number of detectable peaks are reduced and the remaining peaks are easy to identify. Short echo time methods allow more metabolites to be detected, and has better signal-to-noise than long echo time methods. Below is a table showing common metabolites detected by MRS and the TE timescales used to detect them, and Figure 2.5 showing sample spectra at various echo times.

Normally Present	**Detected under abnormal circumstances**
Long TE (strong signal) N-Acetylaspartate (NAA), Creatine (Cr), Phosphocreatine (PCr), Choline (Cho)	*Long TE* Lactate (Lac), pyruvate, Alanine, Glycine
Short TE (strong signal) Glutamate (Glu), Glutamine (Gln), myo-Inositol (mI)	*Short TE* Lipids, macromolecules
Short or Long TE (weak signals) Glucose, Taurine, Glycogen, N-Acetylaspartylglutamate (NAAG)	
Weak signals that can be detected with	

spectral editing techniques Γ-Amino-butyric acid (GABA) Glutathione (GSH)	

Table 2.4 Common compounds detected by MRS in the brain

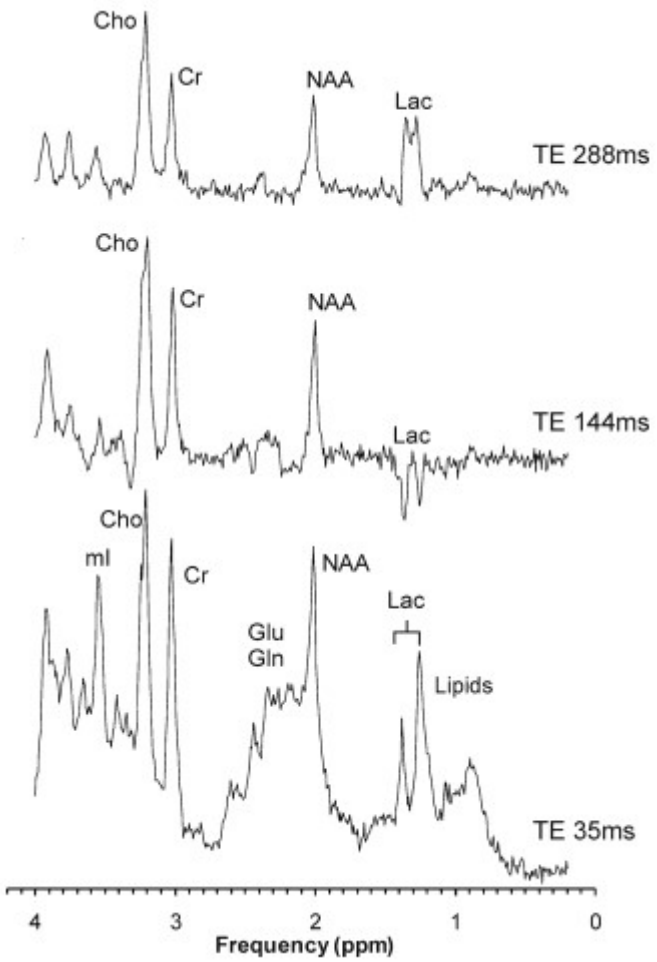


Figure 2.5 Three single voxel spectra of the same ROI acquired using a PRESS sequence with TE=35ms, TE=144ms, TE=288ms. Adapted from[13]. Different metabolite signals can be observed corresponding to what is presented in Figure 2.4

2.4 In vivo NMR spectroscopy in neuroinflammation

Neuroinflammation is defined as an inflammatory response within the brain or spinal cord. It is mediated by the production of chemokines, cytokines, oxygen species, and secondary messengers. It is the cytokines that initiate the flood of other mediators by targeting the endothelium which releases chemokines. Cytokines are small proteins that are involved in cell signalling as they can affect the behaviour of other cells. There are both pro-inflammatory and anti-inflammatory cytokines. Examples of pro-inflammatory cytokines include tumour necrosis factor alpha (TNF-α) and interleukin (IL)-1. IL-4 and IL-10 are examples of anti-inflammatory cytokines whose role is to block the activity of pro-inflammatory cytokines.

Cytokines and the other mediators listed previously are produced by resident glial cells in the central nervous system (microglia and astrocytes), endothelial cells (as mentioned above) and immune cells. There are a number of different consequences of these neuroinflammatory responses, including physiological, biochemical, psychological and immune consequences. Neuroinflammation plays an important role in a wide range of diseases including Alzheimer's disease, Parkinson's disease, and Huntington's disease [14] and also in stroke and multiple sclerosis by impacting neuronal dysfunction thus contributing to disease progression.

Microglial activation is considered to be one of the recognized signs of neuroinflammation [15] and is worth mentioning here due to its link to myo-Inositol and the short study which will be described later in this chapter. Microglia are a type of glial cell found in the brain and are the resident macrophages of the CNS. This means they are the primary form of active immune defence in the CNS. In simplified terms, microglial cells main role is in "brain maintenance" as they clean up damaged or unnecessary synapses, neurons along with plaques and other infectious agents. Microglia have two different phenotypes, a resting state during which they perform their normal maintenance duties, and an activated state during

which they alter their gene expression enabling them to produce more mediators in response to a pathological change in the CNS.

Proton magnetic resonance spectroscopy has been applied to numerous clinical and preclinical studies. It has proved to be particularly useful in non-invasively analysing brain metabolites and therefore is of great interest to our group's focus on neuroinflammation.

Commonly assessed metabolites using MRS include Glutamate (Glu) and NAA (N-acetylaspartate) which are both neuronal markers, Myo-Inositol (mI) is also looked at due to its role as a glial marker. A variation in the concentrations of these metabolites can be used as a biomarker of the severity of a particular brain disorder. In the following paragraphs I will give a brief summary of these metabolites of interest.

Myo-Inositol- It is one of the most abundant metabolites found in the human brain. It is found in glial cells and its concentration levels are thought to be altered in many brain disorders. Myo-inositol has 6 proton containing hydroxyl groups and has resonances between 3.5-4 ppm. Although its exact function is unknown, it has been proposed as a glial marker [16]. This is due to it being present in higher concentration during microglial activation. This alteration of the concentration of myo-inositol has been seen clinically in the form of a higher concentration in Alzheimer's disease [17] and in grading brain tumours [18].

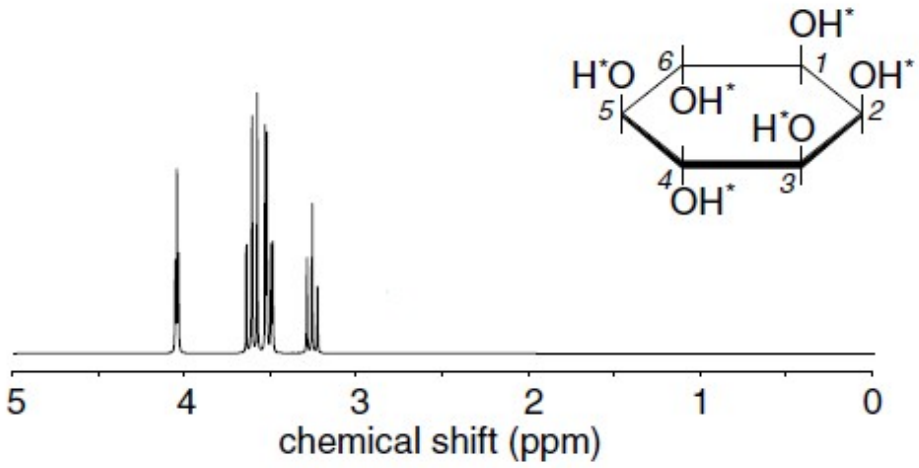


Figure 2.6 Chemical stucture for myo-inositol and simulated NMR spectrum showing clearly its four main resonances; the doublet-of-doublets centred at 3.52 ppm, the triplets at 3.61, 3.27 and 4.05ppm. Adapted from[19].

NAA- In a normal spectrum of human tissue acquired using ^{1}H MR spectroscopy the most visible resonance comes from the methyl group of N-Acetyl Aspartate (NAA) at 2.01 ppm. It is only found in the nervous system and like myo-inositol its exact function is still unknown. Originally ideas about its functions have included the breakdown of NAAG [20] and osmoregulation[21] and most recently Schneider et al [22] have proposed the idea that NAA is a marker of neuronal density. Reduced levels in NAA have been seen in patients with multiple sclerosis [23], Alzheimer's disease and in certain stages of stroke [24]. Because of its link to many diseases like those listed above, NAA is an extensively studied metabolite in MR spectroscopy.

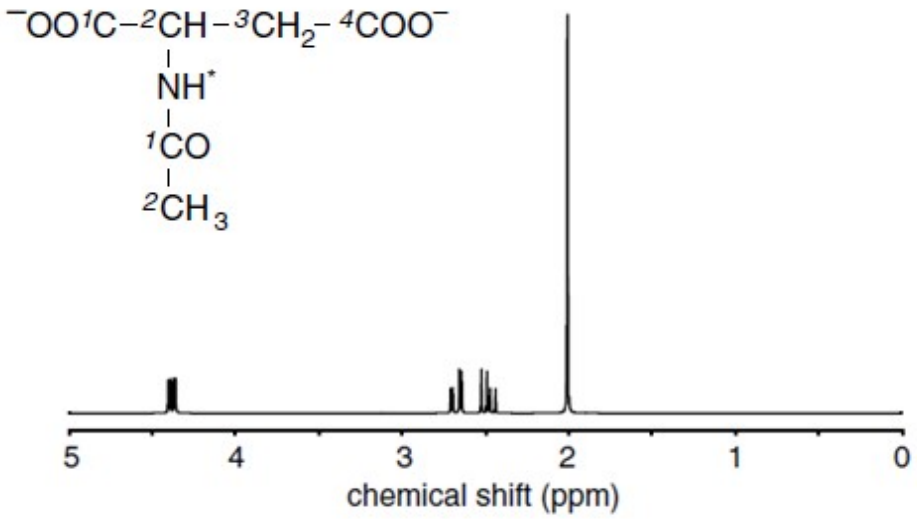


Figure 2.7 Chemical structure for NAA and simulated NMR spectrum showing most prominent peak from methyl group at 2.01ppm along. Smaller resonances are seen as doublet of doublets at 2.49 and 2.67ppm. Adapted from[19].

Glutamate- Another metabolite of great interest for in vivo MR spectroscopy studies is glutamate. Glutamate is a nonessential amino acid, and was shown by a study from Erecinska et al [25] to be a major neurotransmitter in the brains of mammals. It is also a direct precursor of GABA, which is a major inhibitory neurotransmitter. It has a complex NMR spectrum that is difficult to resolve unless high field strengths are used. It is hard to distinguish from Glutamine and so they are often expressed together as Glx.

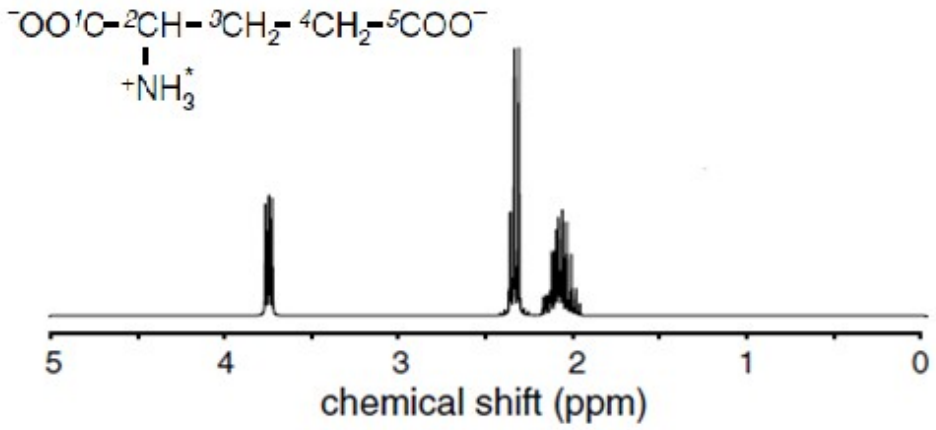


Figure 2.8 Chemical structure and simulated NMR spectrum for Glutamate. It has a complex spectrum with signal from the methine proton appearing as a doublet-of-doublets at 3.75 ppm, and resonances from the other four protons appear as multiplets between 2.04 ppm and 2.35 ppm. Adapted from[19] .

2.5 Investigating the metabolic response in the mouse brain after LPS administration using MR spectroscopy

Through MR spectroscopy we have a tool that allows us to non-invasively monitor alterations of metabolite levels in the brain. This ability to measure the concentration levels enables us to look at key metabolites of interest and how they change. Changes at the molecular level may occur before structural changes can be observed using imaging in the progression of diseases, which means there is a chance to learn more about the early onset of neuroinflammatory diseases using MRS.

The main aim of this study was to monitor the metabolic response in the mouse brain after administration of a neuroinflammatory stimulus (Lipopolysaccharide). Lipopolysaccharide (LPS) is a bacterial endotoxin and is commonly used to activate microglia through stimulation of Toll-Like Receptor 4 (TLR4) which induces secretion of inflammatory mediators causing neuroinflammation [26]. MR spectroscopy and histology were the chosen methods for evaluating the effects of neuroinflammation [27] . MRS can provide us with information regarding the concentration of metabolites linked to neuroinflammation, while histology data can identify microglia which are involved in neuroinflammation. Both wild type mice and a transgenic model of Alzheimer's disease (AD) mice were used. Neuorinflammation contributes to the onset and progression of Alzheimer's disease [28] and as such it was of great interest to see how metabolite concentration levels altered in an AD mouse model.

It was hypothesized that there would be an increase in myo-Inositol levels after LPS administration. It was expected that this would reflect the theory that myo-inositol levels should increase during neuroinflammation as it has been proposed as a glial marker [16]. This is due to it being present in higher concentration in microglial activation.

During microglial activation, microglia cluster together and thus there is an increased concentration of myo-inositol in the hippocampus. Therefore the volume of interest for MRS was focused on the hippocampus as the effects of AD are seen here before other regions of the brain [29, 30].

2.6 Methods

Overview

For this study, APPswe/PS1dE9 (APP/PS1) transgenic mice and wild type C57BL6/J (WT) mice were used. Five mice were used in total, three transgenic and two wild type. These mice were acquired from the Biomedical Service Unit at the University of Nottingham. Lipopolysaccharide was administered intravenously in the lateral tail vein after anatomical MRI images, and baseline MR spectroscopy data has been obtained. Once placed under anaesthesia, the breathing rate and body temperature were monitored throughout the experiment. All MR data was acquired using a Bruker horizontal 7T system with Paravision 5.1 Software and Topspin 2.0(Bruker BioSpin GmbH, Ettlingen, Germany). A 72mm volume coil was used for excitation and a mouse head coil for signal detection. Once all the MR data had been collected, the animal was immediately euthanized by decapitation and the brain was extracted for histology. MR spectroscopy data was then analysed using LCModel [31].

Note-All procedures were approved and met the requirements of the UK Animals (Scientific Procedures) Act 1986.

Experimental Procedure

Dr Marie Christine Pardon (School of Life Sciences, University of Nottingham) weighed the animals, induced them with anaesthesia, and then brought them to the scanner where they were positioned appropriately in a custom made holder. Dr Pardon then connected a catheter to the tail vein, and the i/v line was connected. Body temperature was monitored using a rectal temperature probe and warm water was pumped around the holder to keep the temperature stable (~37˚). The respiration rate was monitored using a pressure plate placed beneath the animals' chest. Both the body temperature and respiration rate were displayed on a screen next to the scanner command console and were noted every 10minutes.

Tuning and matching was performed and checked using the “wobble” command. Anatomical images were acquired in the coronal, sagittal and axial orientations using a RARE (Rapid Acquisition with Relaxation Enhancement) [32] sequence. This sequence used the following parameters; TE=11.8 ms, TR=5 ms, matrix size=256 x 256, Field of view (FOV) =15 x 20 x 30 cm. A global fieldmap shim was performed; this was followed by placing a spectroscopy voxel of 2 x 2 x 2 mm at the hippocampus (see Figure 1.9 below) and then using a local shim. The combination of both shims was to optimize field homogeneity and improve the linewidth.

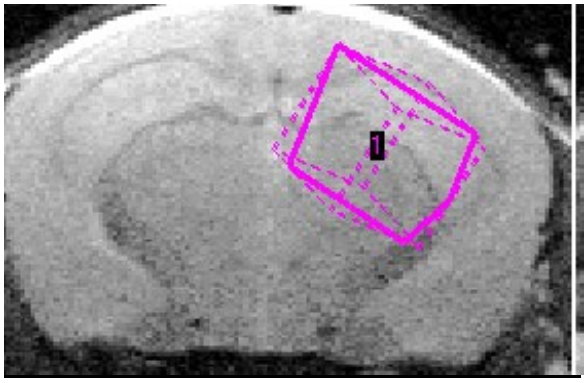


Figure 2.9 Sample anatomical image showing placement of spectroscopy voxel at the hippocampus

The quality of the shim was then examined, by measuring the full width half maximum using a modified PRESS sequence (with geometry imported from local shim) that had no water suppression. The average linewidth across all mice used for this pilot study was 9.5Hz for our volume of interest. If the shim was not deemed adequate, then one would have to run the local shim and measure the full width half maximum again as described above. Finally spectra were obtained using a PRESS sequence which had the following parameters; TR/TE = 2500/13ms, 512 averages, 8 dummy scans. 2048 data points, spectral width 4006 Hz and water suppression (bandwidth 200Hz). A reference without water suppression was also taken.

The steps described in the previous paragraph were performed for two baseline spectroscopy scans. Mice were injected with LPS dose (300µg/kg), and spectra were

acquired every hour by again repeating the steps described in the previous paragraph. Mice were taken out of scanner by Dr Pardon, who then killed them immediately and extracted their brains for histology.

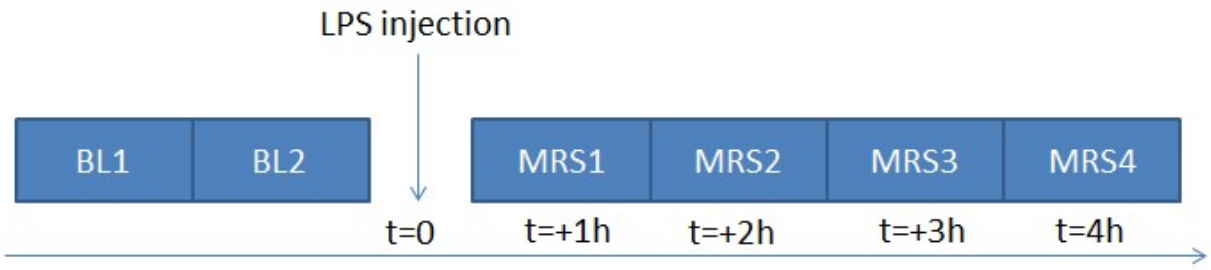


Figure 2.10 Timeline for MRS where BL1 and BL2 are the baseline spectra taken prior to LPS injection and MRS1-4 are the spectra taken post LPS injection

Shimming

Because spectral resolution and SNR are both affected by B_0 nonuniformities, optimization of B_0 shimming is crucial in MR spectroscopy. Although the T_2 of the metabolites define the spectral linewidth, the true linewidth is defined by the B_0 shim. B_0 shimming can be adjusted by changing the static electrical currents through external coils, which affect the B_0 field spatially. B_0 maps are acquired using MR sequences obtained with at least two different TEs, either from the entire volume, or from several rods through the voxel (FASTMAP) [33]. These maps are then fitted to the known harmonics of the shim fields, from which the required current can be calculated.

^{1}H *in vivo NMR Spectroscopy quantification using LCModel*

Automatic quantification of *in vivo* proton MR spectra using LCModel [31] is used to estimate metabolite concentrations. This enables us to compare these concentration values between what is normal and abnormal. Metabolite concentrations are obtained using LCModel quantification algorithm based on the nonlinear Levenberg-Marquardt iterative algorithm. This algorithm analyses the *in vivo* spectrum as a linear combination of individual *in vitro* metabolite spectra that constitute a basis set. The *in vitro* basis set is modified to take into account the following differences between the *in vitro* and *in vivo* data; frequency shift from possible referencing errors, a baseline, convolution due to eddy currents and field inhomogeneities, and zero and first order phase corrections for the *in vivo spectra*. A constraint regularization method accounts for differences in the baseline, phase, lineshapes and makes an estimation of the metabolite concentrations and the corresponding uncertainties associated with these measurements. It is fully automatic with the *in vivo* time domain data being the only requirement. The basic operating steps for LCModel are shown in the figure below.

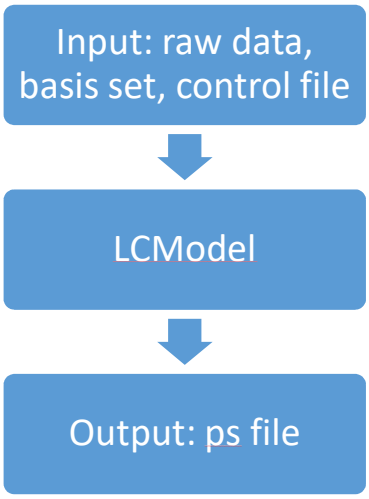


Figure 2.11 Operating procedure for LCModel where the raw data is what you acquired on the scanner, the basis set is a set of simulated individual *in vitro* metabolite spectra and the control file contains your parameters for analysis

Below is a sample ps file from LCModel showing; the raw data fit, LCModel fit, baseline (contribution of protons not accounted for in analysis), residual (raw data minus LCModel fit) and the metabolites along with their corresponding concentration ratios to total creatine, absolute concentration and their Cramer Rao Lower Bounds (%SD).

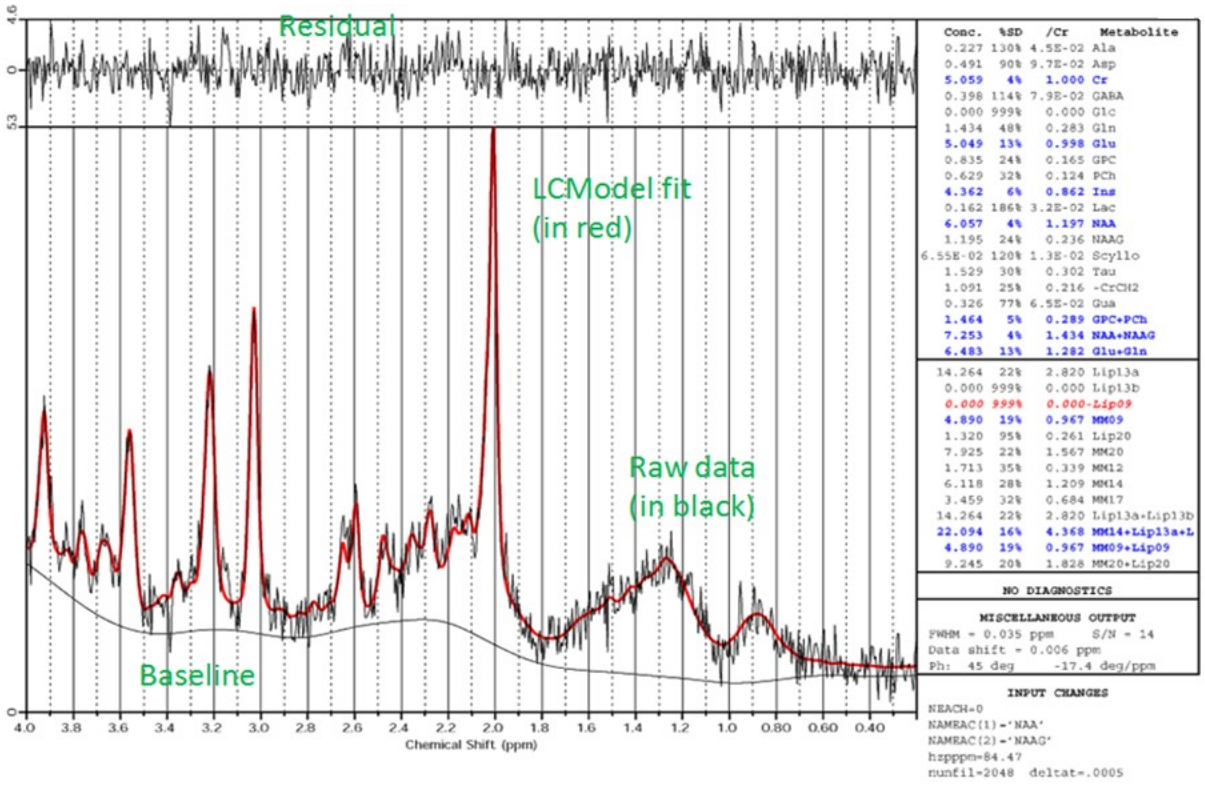


Figure 2.12 Summary of LCModel output

Although LCModel was the chosen analysis software for this set of experiments it is worth noting that it has some drawbacks including the cost (£8,000) and limited customisation. There are many other MR spectroscopy analysis software, such as TARQUIN which have their relative merits and drawbacks. However LCModel was chosen for this study as it is used widely, accepts most scanner manufacturers data, there are extensive publications on the methodology, and the manual and technical support are excellent.

2.7 Results

In both wild type (WT) and AD mice, an increase in myo-inositol values was observed post LPS injection, which were quantified using LCModel, these values increased over time as can be seen in Figure 2.13 and Figure 2.14. In WT mice there was a mean 10%±2% increase in the first two hours. A mean 20%±3% increase in myo-inositol concentration values post LPS injection was observed in AD mice.

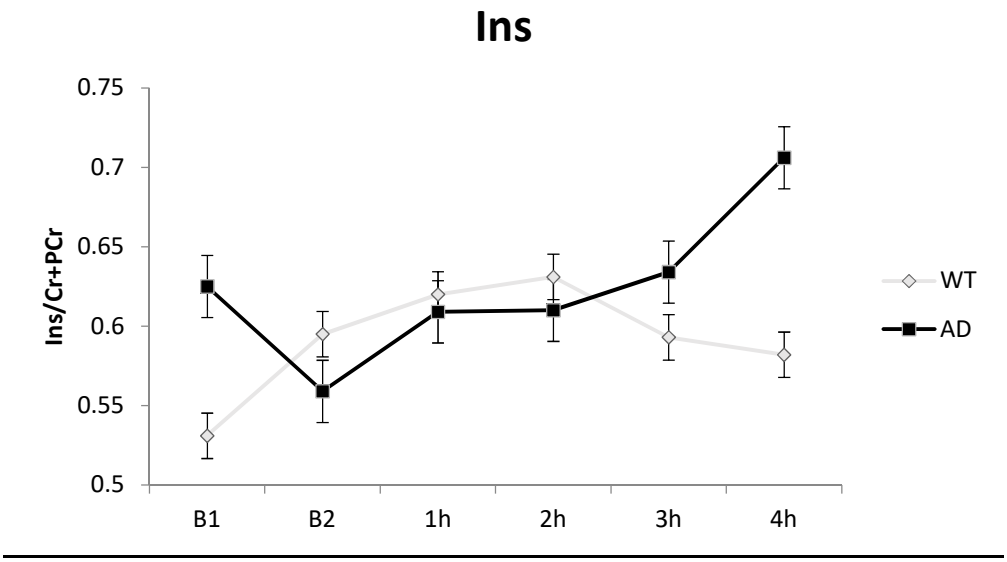


Figure 2.13 Variation of Ins/Cr+PCr over time in both AD (n=3) and WT(n=2) mice where B1 and B2 are baseline spectra taken prior to LPS injection, subsequent spectra were taken every hour post LPS injection for four hours. Error bars shown as standard error of the mean.

There was a much greater increase of myo-inositol levels for AD mice, and this can be seen quite clearly in the figure below.

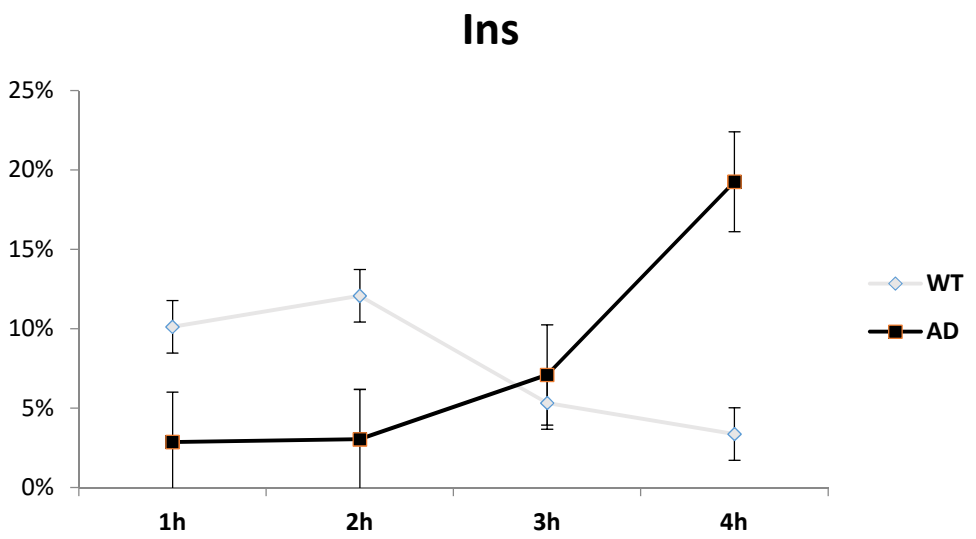


Figure 2.14 Percentage change of myo-inositol for AD and WT mice post LPS injection. Error bars shown as standard error of the mean.

Both figures were based on mean values of mI relative to total creatine (mI/Cr+PCr) from all subjects used for the study at the relevant time points. With regards to the rest of the metabolite levels measured, a decrease in both taurine and NAA was seen. A sharp decrease in NAA was noticeable after the first hour (post injection) in the LPS treated AD mice. Taurine levels decreased with time, and this was especially evident in the AD mice.

2.8 Discussion and Conclusion

From the MRS data, changes in the levels of myo-inositol can clearly be seen across the entire group after LPS administration. In WT mice there was an increase in myo-inositol levels within the first two hours, before myo-inositol levels decreased which is something to be considered for future studies, as perhaps if a larger dose of LPS had been administered then this value would have linearly increased over time. A greater increase in myo-inositol concentration values post LPS injection was observed in AD mice. This larger increase agrees with the hypothesis of myo-inositol increasing during microglial activation, with AD sufferers being more susceptible to this [34] which might also explain the greater standard deviation in the AD group.

Perhaps a suitable follow up to this experiment would be to increase the sample size, and use a higher dose of LPS. This of course would have to be in agreement with what is seen in behavioural studies of the mice after LPS injection, as to avoid the chance of the animals being made too “sick” after the injection and thus potentially decreasing their chances of surviving the experiment. It is also worth considering the effect of the chosen anaesthesia use for this study. Studies have shown that exposure to anaesthesia (both prolonged and short) can have an impact on the metabolite levels [35] , so perhaps in a follow up experiment, a different form of anaesthesia could be used.

It can be seen from this pilot study that MRS myo-inositol measurements have the potential to be used as a biomarker for microglial activation provided the histology data agrees with the MRS data acquired, however further studies are needed to validate this hypothesis.

3 Deuterium relaxation times in D_2O mixtures

3.1 Introduction

The aim of this work was to investigate whether D_2O could be a feasible contrast agent for *ex-vivo* lung imaging. ^1H MRI of the lungs is challenging, owing to the fact that the lungs consist mostly of empty space, lacking the density of protons required to contribute to sufficient MR signal. Strategies for motion correction must also be employed when imaging the lung using MRI. Through the use of D_2O, perhaps sprayed on to the lungs using a nebulizer, offers the possibility of imaging the distribution of D_2O in the lungs and by utilizing a deuterium NMR probe we can ensure that what is observed is only the signal from the D_2O. This gives this methodology specificity which conventional MRI methods often lack.

Deuterium oxide (D_2O) is a form of water in which both hydrogen atoms are substituted by deuterium. D_2O has been utilized in MRI as an exogenous diffusible tracer for *in vivo* MRI perfusion experiments[36]. D_2O has chemical and physical properties that are very similar to that of H_2O , however it is undetectable in conventional NMR owing to its different resonance frequency. Deuterium is a promising nucleus for magnetic resonance *in vivo* due to its negligible background signal in biological tissue which makes the origin of the signal easy to detect. It also has low toxicity and D_2O is commercially available.

Below is a table comparing the NMR properties of proton and deuterium atoms.

Comparing properties of Proton and Deuterium

	Proton	Deuterium
Natural Abundance	99.985%	0.015%
Gyromagnetic ratio (γ)	26.7519 x 10^7rad T^{-1} s^{-1}	4.1066 x 10^7rad T^{-1} s^{-1}
Resonance Frequency (@9.4T)	399.7158 MHz	61.3584 MHz
Spin	1/2	1

Table 3.1 A comparison of the NMR properties of the proton and deuterium nucleus

In this work T_1 and T_2 values of D_2O and D_2O mixtures were obtained for various samples. In its simplest terms, T_1 is the time constant describing the regrowth of longitudinal magnetization M_z after application of an RF pulse. It is the rate of the spin system returning to thermal equilibrium with the surrounding spins. T_1 relaxation (also known as longitudinal or spin-lattice relaxation) stems from the interaction of the microscopic magnetic field of the nucleus of interest with the microscopic magnetic fields of nuclei in the surrounding environment/lattice. This causes small magnetic field fluctuations to build a net magnetization along the xy plane (direction of applied magnetic field).After a while this net magnetic field no longer changes and thermal equilibrium is reached. T_2 is the time constant describing the decay of transverse magnetization M_{xy}. After application of a 90° RF pulse to the bulk magnetization, the magnetization will then precess at the Larmor frequency in the xy plane. However, slight variations in the precession of each nucleus caused by small differences in the magnetic field induced by neighbouring spins will cause the irreversible decay of the transverse magnetization.

3.2 Methods

The experiments were carried out with a 400MHz Oxford NMR spectrometer using an in-house built ^2H probe. The T_1 and T_2 values were determined using an inversion recovery (IR) and Carr-Purcell-Meiboom-Gill (CPMG) sequence respectively.

Preparation of samples

A set of samples were prepared by adding a certain volume of D_2O to a modified Eppendorf Tube so that the total volume was 1ml. Appropriate calculations were made to give us three different samples; pure D_2O, isotonic solution containing 14% D_2O, and a water solution containing 17% D_2O. Another sample was made by soaking some raw chicken in a D_2O + saline solution overnight to replicate similar conditions of tissue. All samples were contained in 1.5ml Eppendorf tubes that had been modified to fit the coil used for these experiments.

Measurement of relaxation times

As mentioned above, the experiments were carried out with a 400MHz Oxford NMR magnet using a Kea spectrometer with Prospa software. T_1 measurements were made using a T_1-Inversion Recovery pulse sequence (shown in Figure 3.2). In this 2-pulse experiment, a 180° pulse is applied to the system, causing the spin population to be inverted, therefore leaving no magnetization in the xy plane. The system is then allowed to approach equilibrium for a predefined delay, a 90° pulse is then applied which rotates the z-magnetization that had recovered during the delay into the xy plane. The magnitude of the FID (measure of magnetization) at this point is recorded. This is repeated for a range of interpulse delays and then the magnetization values are plotted against the delays fitting to a curve of the form $M=M_0\{1-2\exp(-t/T_1)\}$ to give T_1.

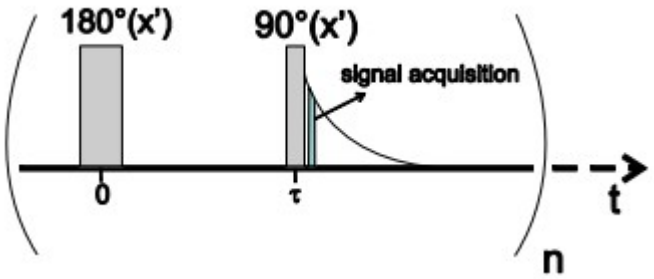


Figure 3.2 Inversion-recovery sequence for the measurement of T_1

T_2 measurements were made using a Carr-Purcell-Meiboom-Gill (CPMG) pulse sequence (shown in Figure 3.3). This consists of a train of RF pulses (90°-delay-{180°-delay}$_n$) with each pulse having the same pulse width. Between each pair of pulses an echo is collected. Each of these echoes is integrated and fitted to a curve of the form $M=M_0\exp(-t/T_2)$ to give T_2.

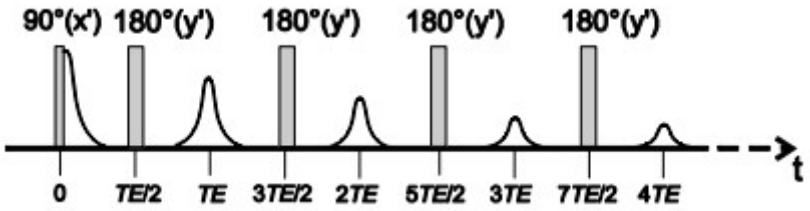


Figure 3.3 CPMG sequence for the measurement of T_2

3.3 Results

Table 3.4 shows both T_1 and T_2 values and standard deviation over the samples for three different types of sample. Sample T_1 and T_2 curves for the raw chicken soaked in D_2O + saline solution are shown in Figures 3.5 and 3.6. Sample curves for T_2 values of the different samples in Table 3.4 are shown in Figures 3.7-3.9.

Sample	T_1 (msec)	T_2 (msec)
Pure D_2O	296±7 ms	331±3 ms
Isotonic solution containing 14% D_2O	367±3 ms	436±18 ms
Water solution containing 17% D_2O	355±3 ms	421±14 ms

Table 3.4 T_1 and T_2 values of the three different samples

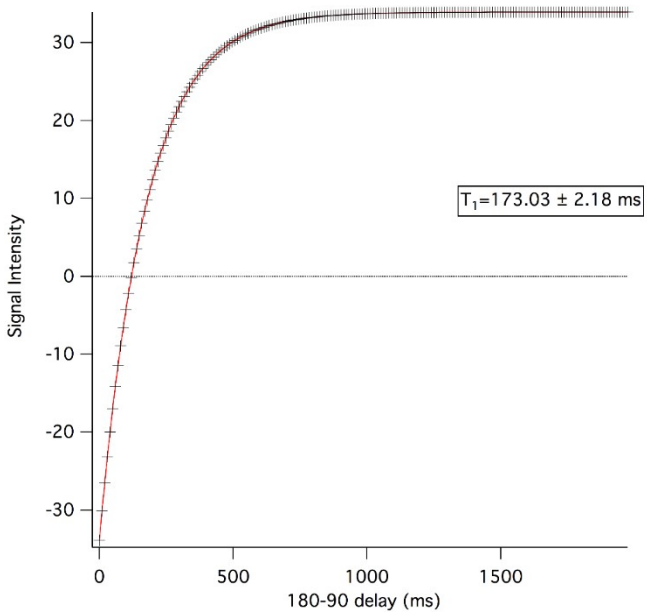


Figure 3.5 Sample T_1 curve with average value given from "tissue sample"

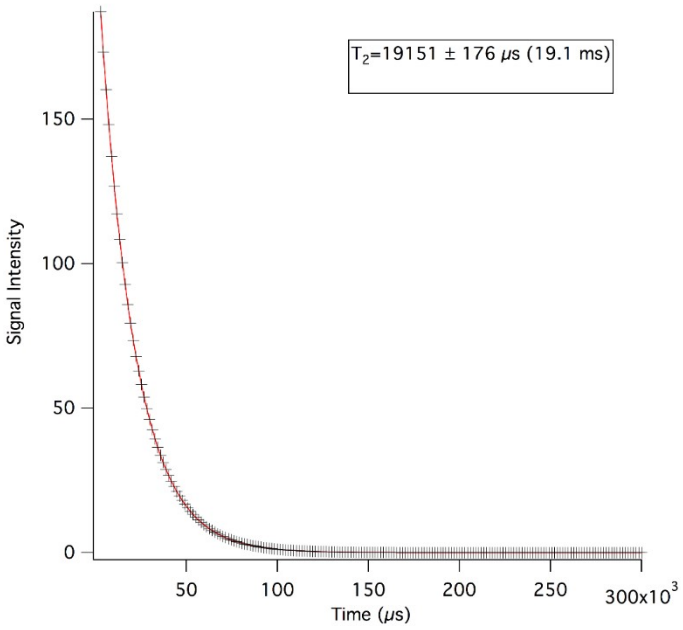


Figure 3.6 Sample T_2 curve with average value given from "tissue sample"

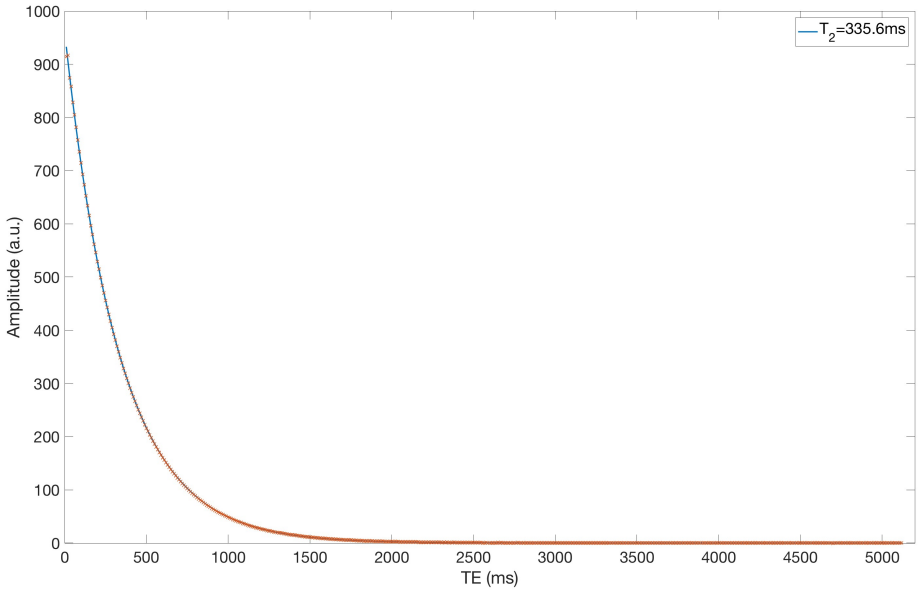


Figure 3.7 Sample T_2 curve of pure D_2O sample

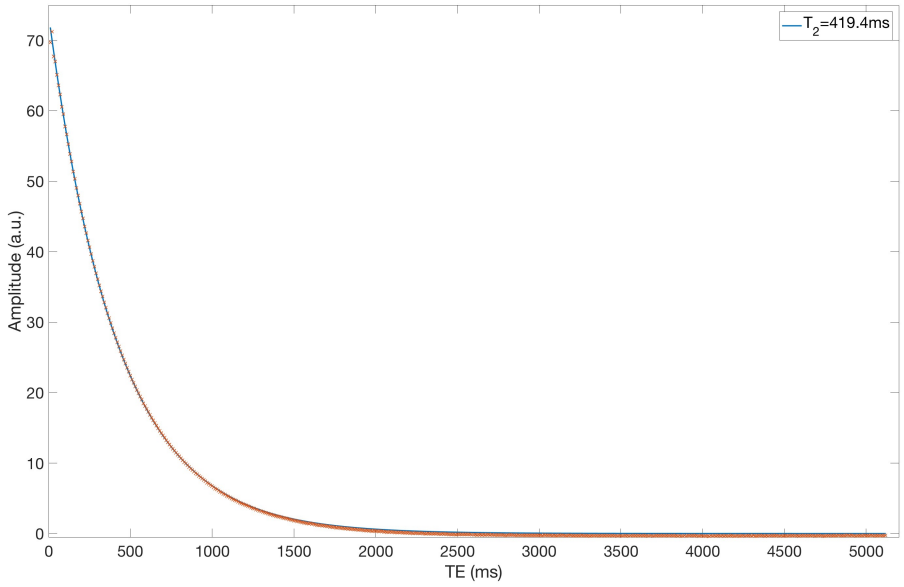


Figure 3.8 Sample T_2 curve of isotonic solution containing 14% D_2O

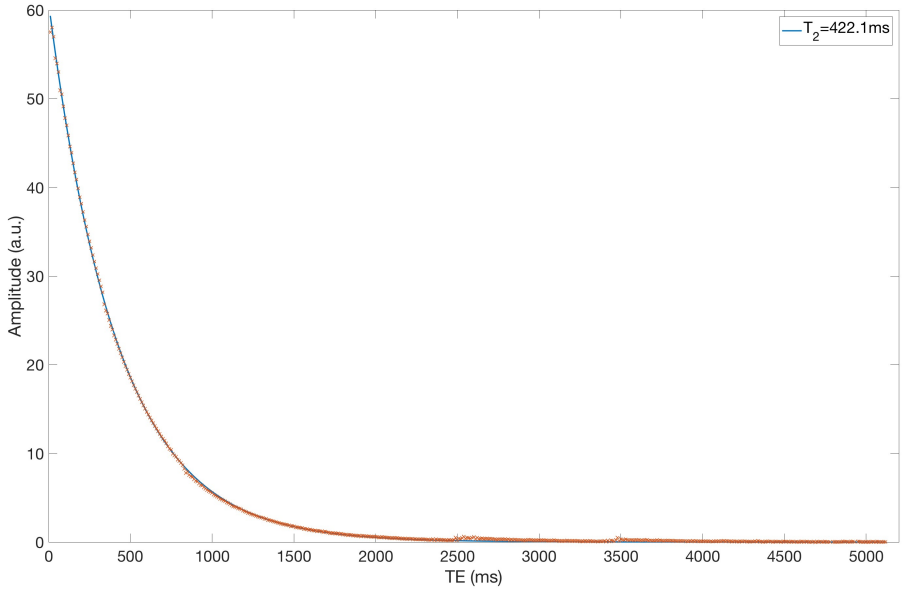


Figure 3.9 Sample T_2 curve of water solution containing 17% D_2O

3.4 Discussion and Conclusion

Figure 3.4 showed a trend of T_2 values longer than T_1 values which defies common logic in NMR, as everything causing T_1 relaxation also causes T_2 relaxation and some T_2 processes do not involve T_1 meaning $T_2 \leq T_1$ always. Perhaps this was due to an error in one of the pulse sequences, but it's still inconclusive as to what caused these erroneous values.

Values for the "tissue" sample however, did follow the correct trend. T_1 values on average were 173ms and T_2 values on average were 19ms. One possible explanation for the observation of these short T_1 values was that magnetic field inhomogeneities had some influence, but spin echo theory in NMR states that this cannot be the case. The only remaining hypothesis which fits is that as deuterium is a quadrupolar nuclei its dominant relaxation mechanism must be due to the interaction of the quadrupole electric moments of its nuclei with surrounding electric field gradients. This may also explain why the relaxation values found in this study were shorter in the "tissue" sample compared to the liquid samples, as electric field gradients in a liquid (water) are small due to the random orientation of the electric dipoles which means the electric field at any time and position averages to zero. However, in a tissue structure where there is more order, this averaging will be reduced and thus the electric field gradients will be increased meaning more rapid NMR relaxation of deuterium.

Based on the short T_2 values it was decided not to continue with this work, as there would be challenges associated with imaging a sample with such a short T_2 which leads to low signal intensity. Recent advances in MRI technology and hardware means short-T_2 imaging can be achieved with techniques such as ultra-short echo time (UTE) and zero echo time (ZTE) imaging, however it was beyond the scope of this project to develop and optimise these.

4 Targeted hyperpolarized ^{129}Xe biosensors

4.1 Introduction

Through hyperpolarization, it is possible to achieve a massive signal enhancement when compared to conventional MRI at thermal equilibrium conditions. When used in conjunction with a biosensor, greater sensitivity and specificity are achievable. Alexander Pines and his research group at Berkeley pioneered the concept of a xenon MRI biosensor in 2001[37] . Their sensor used a biotin labelled cryptophane construct that enabled the detection of streptavidin at much lower concentrations than those achieved in conventional MRI contrast enhanced experiments. Since then, the field of ^{129}Xe biosensors has grown rapidly with sensors measuring a wide range of biological processes based upon the activity of proteins, enzymes and even cells.

This section contains a literature review of developments in hyperpolarized ^{129}Xe biosensors over the past couple of years. Firstly, an introduction will be given describing what a biosensor is accompanied by a brief overview of the field of hyperpolarized ^{129}Xe.

The hyperpolarization method used in our lab and research carried out in our lab until now in the area of hp ^{129}Xe MRI will also be presented. A description of HYPER-CEST[38] which many groups utilise to significantly lower the detection limits of their biosensor will be given, and finally an overview of the different sensors paying particular attention to the xenon host molecule(s) will be presented. Overall, this section aims to summate the hyperpolarized ^{129}Xe biosensor literature to identify any knowledge gaps or technical approaches that could be pursued in future research.

4.2 ^{129}Xe Biosensors

Unlike general contrast agents, biosensors aim at specific biological events. This includes events such as changes in enzyme activity. These biosensors can take various forms but broadly speaking, a xenon biosensor consists of a xenon host molecule (cryptophaneA for example), a linker and a targeting moiety. This targeting moiety or functionalized unit is usually enzyme or receptor specific.

Due to the sensitivity of xenon to its chemical environment, this makes it possible to detect a biosensor owing to its unique resonance frequency in solution compared to free xenon. The binding of a sensor to its molecular target is also detected in a similar vein, and the concept mentioned above is shown below in Figure 4.1.

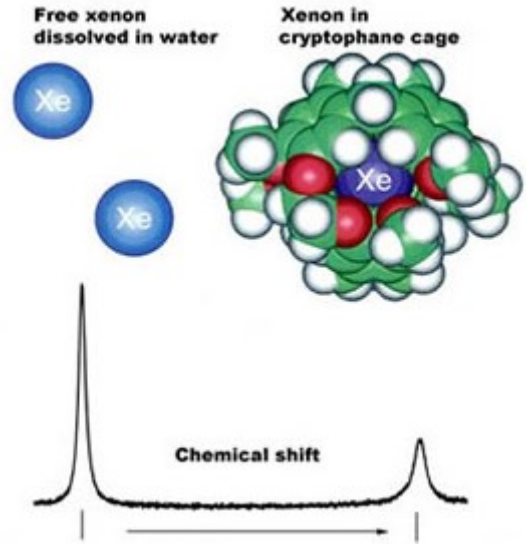


Figure 4.1 Concept of ^{129}Xe biosensor showing different NMR signal for free and caged xenon. Adapted from [39].

MRI biosensors can usually be classed as pH sensors, enzyme sensors, or ion sensors. pH sensors are of great interest due to a decrease in pH observed for hypoxic tissue such as that found in certain cancer and metabolic diseases. The chemical shift of xenon is strongly pH dependent, something that was utilized by Riggle et al [40] whose sensor labelled cells in acidic environments. Enzyme sensors are scattered throughout the literature. These sensors consist of molecular target that is sensitive to the presence of a specific enzyme. This has been achieved by Dmochowski's group in UPenn [41] who attached a MMP-7 substrate to a

cryptophane-A xenon host via a linker which could be cleaved. Using this setup they were able to detect changes before and after enzymatic reaction. Ion sensors, in particular those that are zinc based are also dotted throughout the literature. Zinc plays a regulatory role in gene expression and is also found in certain protein complexes and enzymes. Indeed, Ji Zhang et al [42] showed how hyperpolarized ^{129}Xe NMR can be used for zinc ions detection by attaching 2-(diphenylphosphino) benzamine as a ligand to a cryptophane based xenon host. Other groups have looked at detecting toxic metal ions such as Zn2+ along with Pb2+ and Cd2+ [43] which is of great importance as prolonged exposure to ions like these can have adverse effects on health and have been linked to diseases such as cancer.

4.3 ^{129}Xe MRI - background and current developments

In addition to proton (^{1}H), which is used in conventional MRI, other nuclei are also suitable for MRI. One such nucleus is ^{129}Xe which when coupled with hyperpolarization has emerged as a promising candidate for the development of molecular MRI. This isotope of xenon has 26.5% abundance in xenon gas and is widely available. ^{129}Xe is a spin ½ nuclei, which in turn leads to simplified NMR spectra due to having only two energy states. A ^{129}Xe nucleus has a gyromagnetic ratio of 0.6192895 x 10^{7} rad $s^{-1}T^{-1}$. ^{129}Xe is extremely sensitive to its chemical environment and due to its large electron cloud it has a chemical shift of 300 ppm [44] in solution. Multiple xenon species can be resolved simultaneously using NMR as a result of its large spectral range. ^{129}Xe also has good solubility in liquids [45].

Since Albert et al [46] in 1994 first utilised hp ^{129}Xe for lung imaging, this field has undergone rapid developments. Indeed, it has been used in vivo and in a clinical setting. It has been used to look at a wide range of clinically relevant pathologies in vivo including ventilation defects [47], and also in ex vivo [48]. For a comprehensive overview of current developments in ^{129}Xe MRI, the reader is referred to the excellent review article by Lilburn et al [49].

4.4 Hyperpolarization of ^{129}Xe through spin exchange optical pumping

In order to achieve hyperpolarization of ^{129}Xe in our lab spin exchange optical pumping or SEOP is used which can be broken down into two steps: the first step involves the transfer of angular momentum from the circularly polarised laser light (tuned to the D_1 frequency of Rb in our case) to the electron spins of the alkali metal vapour (Rb) and the second step involves transferring the high spin polarization to the nuclei (^{129}Xe) of interest via spin exchange.

When a SEOP cell containing Rb is irradiated with circularly polarized light at 794.7 nm in the presence of a weak magnetic field, the population is driven from m_J=-1/2 in the $^2S_{1/2}$ state to m_J=+1/2 in the $^2P_{1/2}$ state adhering to the selection rule of Δm=+1 as shown in Figure 2.2. Collisional mixing between Rb atoms equalizes the populations in m_J=+1/2 and m_J=-1/2 in the $^2P_{1/2}$ state. This in turn equalizes the repopulation of electrons in the ground state. The return of electrons to the ground state occurs either through non-radiative quenching, or through the spontaneous emission of a photon. The former is preferred as the spontaneous emission of a photon is detrimental to the SEOP process, as it would depolarize the electron spins. It is for this reason a quenching gas such as nitrogen is added to the gas mixture.

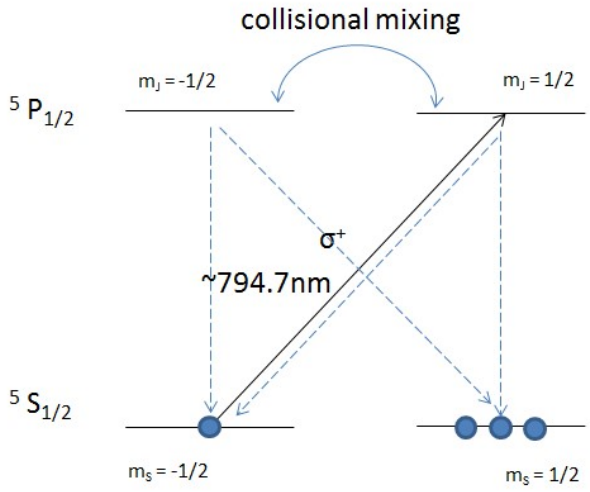


Figure 4.2 Optical pumping of Rb

During the second stage of SEOP, gas phase collisions occur between ^{129}Xe and the polarized Rb atoms. These collisions offer the probability that spin exchange (see Figure 4.3) will occur between the polarized Rb atom and the unpolarized ^{129}Xe atom via Fermi contact hyperfine interactions between the ^{129}Xe gas nuclear spins(I) and the electron spins(S) of Rb.

$$\alpha\vec{S}\cdot\vec{I} = \frac{\alpha}{2}[S_+I_- + S_-I_+] + \alpha S_zI_z \qquad (1)$$

The flip-flop term in the brackets represents the spin exchange between Rb and ^{129}Xe, and alpha gives the probability of finding the valence electron of Rb at the nucleus of ^{129}Xe.

The transfer of angular momentum between Rb and ^{129}Xe occurs either through binary collisions or in van der Waals complexes .The collisions are often three body (due to the presence of nitrogen) and as such the spin exchange rate is given by [50]

$$\gamma_{SE} = \left(\frac{k_{vdW}}{[M]} + k_{SE}\right)[Rb] \qquad (2)$$

Where the van der Waals specific spin-exchange rate for three body collisions is given by k_{vdW} , k_{SE} is the Rb-^{129}Xe spin-exchange rate and [M] and [Rb] are the number densities of the third body gas and rubidium respectively. It can be observed from equation (2) that large spin exchange values can be achieved by reducing the number of third body gas atoms. This means larger van der Waals lifetimes occur at low pressure, reducing the probability of molecular collisions which destroy these van der Waal complexes. For this reason, along with the positive effect reducing pressure has on the polarization of rubidium (spin destruction rate decreased due to fewer Rb-Rb collisions) our lab utilizes a low pressure hyperpolarization setup, details of which can be found in [51].

The probability of a mutual spin flip between the Rb and ^{129}Xe is low , however this is overcome by ^{129}Xe's long T_1's thus the polarization of ^{129}Xe can build up over time, given us an apparent polarization of [50]

$$P_{Xe}(t) = \frac{\gamma_{SE}}{\gamma_{SE}+\gamma_O}P_{Rb}(1-\exp[-(\gamma_{SE}+\gamma_O)\,t]) \qquad (3)$$

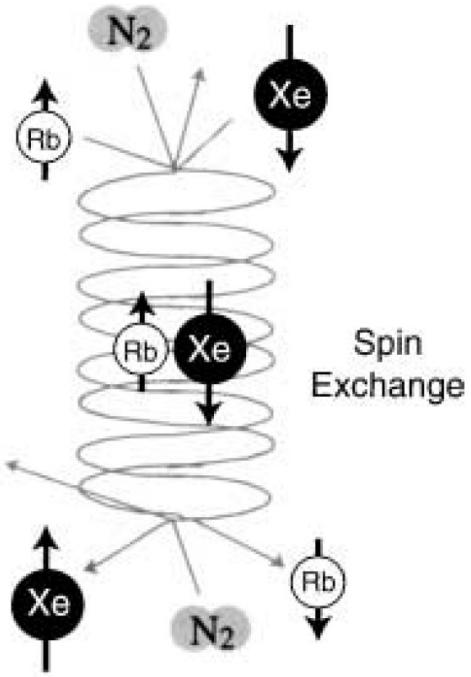


Figure 4.3 Polarization of xenon nuclei via collisions and spin exchange. Taken from [52].

This method enables us to overcome the relatively low sensitivity of NMR, which is one of its major limitations for use in molecular imaging. The polarizer developed here in our lab can achieve xenon polarizations as high as 15%[51] which results in a massive amplification of the signal intensity when compared to thermally polarized nuclei.

4.5 Chemical Exchange Saturation Transfer (CEST)

Ongoing developments in the design of new MRI contrast agents, has led to the design of novel imaging techniques to compliment them. Most of these pulse sequences exploit frequency, it being the key parameter in NMR and MRI.

One interesting form of exploiting the frequency is transferring magnetization or saturation between different chemical environments in order to gain sensitivity enhancement. This was first demonstrated by Balaban's group[53] who showed the chemical exchange between a small solute pool of protons and large pool of water protons. They named this new mechanism chemical exchange saturation transfer (CEST). In their experiments, they used 5,6-dihydrouracil and barbituric acid as the sites for RF pulse saturation. During the CEST experiments, RF irradiation at a specific frequency saturated the proton spins in these compounds. This inverts the spin populations, which is then transferred to a pool of water protons via chemical exchange (which occurs much faster than spin relaxation mechanisms), which results in a reduction of water proton signal intensity (see Figure 4.4).

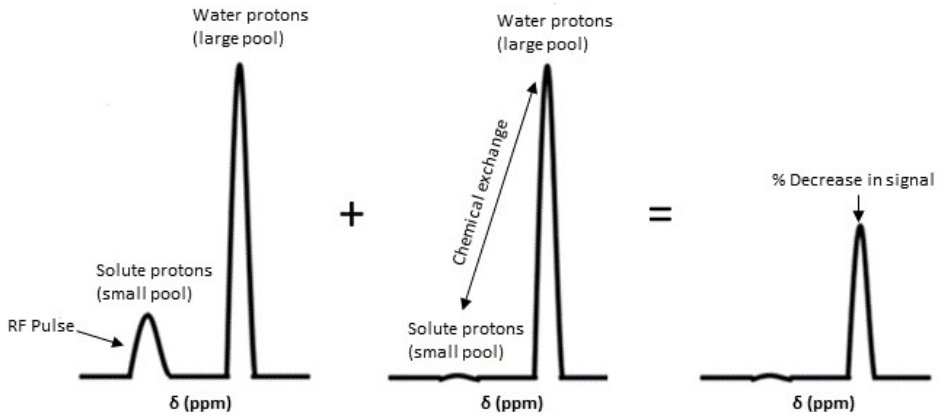


Figure 4.4 Simplified CEST explanation viewed as a proton NMR spectrum. The signal from an exchangeable solute proton that is different from bulk water is reduced *via* a selective RF pulse while the proton is exchanging with protons in the bulk water. These two events result in a reduction of the bulk water signal intensity, which is commonly expressed as a percentage decrease.

Reporting the molecular information associated indirectly with the exchanging species, readouts of CEST experiments are the water signal intensities at different saturation frequencies and RF pulse strengths used. As a result of this indirect detection method it is possible to gain a 500,000 times greater sensitivity enhancement [54] due to the strength of the water signal relative to any other proton species being investigated.

4.6 HYPER-CEST with ^{129}Xe

CEST can also be applied to hp ^{129}Xe and is known as HYPER-CEST. This was first shown by Leif Schroder et al[38] . When used with a ^{129}Xe biosensor, HYPER-CEST can solve the intensity and contrast problems often found in MRI. Biosensors are found at low concentrations, something which HYPER-CEST can overcome using indirect detection. In HYPER-CEST, free hp ^{129}Xe in solution is used to detect a dilute pool of hp ^{129}Xe bound to a biosensor. This is achieved by irradiating the bound pool with a selective RF saturation pulse. The resulting induced depolarization is then transferred via chemical exchange to the free hp ^{129}Xe in solution followed by detection of the free hp ^{129}Xe for which the spin polarization has been decreased, at the same time fresh hp ^{129}Xe atoms are being transferred into the trapped xenon. Overall this method results in an amplification of the bound hp ^{129}Xe signal which enables its detection at nanomolar/picomolar concentrations. A typical HYPER-CEST pulse sequence as shown in Figure 4 consists of an RF saturation pulse of power B_1 with frequency ω_{sat}, followed by a readout of the remaining magnetization. The readout can be an imaging sequence such as GRE, EPI or it can be a spectroscopic readout (90° pulse followed by FID acquisition).

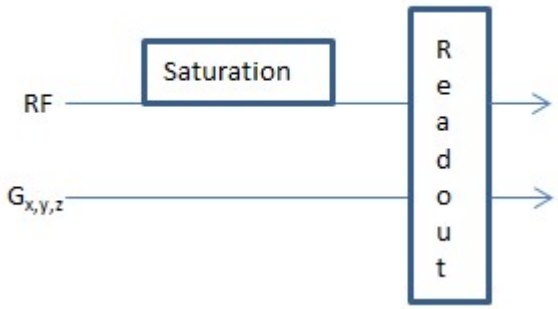


Figure 4.5 A simplified version of a HyperCEST pulse sequence

CEST effects, both quantitative and descriptive are usually described by the Bloch-McConnell equations [55]. Consider a two pool model consisting of free ^{129}Xe in solution (index f) and ^{129}Xe bound to the biosensor (index b) with a continuous

wave RF saturation pulse having field strength $\omega_1 = \gamma B_1$ applied along the x-axis, giving

$$\frac{dM_x^f}{dt} = \Delta\omega_f M_y^f - R_2^f M_x^f - k_{fb} M_x^f + k_{bf} M_x^b$$

$$\frac{dM_x^b}{dt} = \Delta\omega_b M_y^b - R_2^b M_x^b - k_{bf} M_x^b + k_{fb} M_x^f$$

$$\frac{dM_y^f}{dt} = \Delta\omega_f M_x^f - R_2^f M_y^f - k_{fb} M_y^f + k_{bf} M_y^b - \omega_1 M_z^f$$

$$\frac{dM_y^b}{dt} = \Delta\omega_b M_y^b - R_2^b M_y^b - k_{bf} M_y^b + k_{fb} M_y^f - \omega_1 M_z^b$$

$$\frac{dM_z^f}{dt} = -R_1^f \left(M_z^f - M_0^f\right) - k_{fb} M_z^f k_{bf} M_z^b + \omega_1 M_y^f$$

$$\frac{dM_z^b}{dt} = -R_1^b \left(M_z^b - M_0^b\right) - k_{bf} M_z^b k_{fb} M_z^f + \omega_1 M_y^b \qquad (4)$$

Where $M_{x,y,z}^{f,b}$ are the magnetization vector components in either the bound or free xenon pools, $\Delta\omega_{f,b}$ is the difference between the saturation pulse frequency and the frequency of either of the pools, $R_{1,2}^{f,b} = \frac{1}{T_{1,2}}$ and $k_{bf,sc}$ are exchange rates constants between pools. These exchange rate constants must be less than or equal to the difference in frequency between the two exchange sites.

4.7 Xenon Hosts

When designing a xenon biosensor, special attention must be given to the xenon host moiety. Two crucial requirements are: 1) It should have a high binding affinity for xenon and 2) The reversible exchange between xenon atoms trapped in the cage and those outside it, must be fast enough to allow efficient CEST detection. Various constructs have been proposed as xenon hosts, including cucurbit-[n]-urils[56, 57] gas-vesicles [58], metallosupramolecular cages[59] and cryptophanes [42, 43, 60-73]. Of these, cryptophane-A (CrA) is the most favoured xenon host due to its favourable properties which will be mentioned below.

Crypthophane-A (CrA)

Cryptophane-A has a large affinity for xenon gas, and its reversible exchange interaction is on the desired timescale for HYPER-CEST. It also gives a huge shielding effect to the caged xenon, meaning there is a large chemical shift between the caged and free xenon. The xenon-cryptophane interaction has been well studied [74]. The cavity size of CrA is 95 $Å^3$ giving it the ideal ratio between guest volume and host volume when used with xenon which has a van der Waals volume of 42 $Å^3$ [75]. This gives it favourable xenon binding and exchange characteristics for HYPER-CEST [38] .

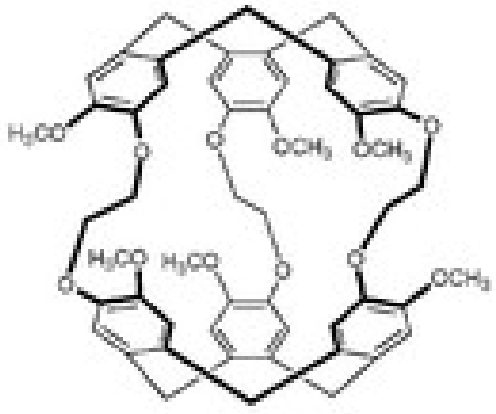


Figure 4.6 Cryptophane-A. Adapted from [76].

Concluding remarks

The application of in vivo NMR spectroscopy to provide a non-invasive biomarker for neuroinflammation, and the use of selected contrast mechanisms to improve the sensitivity and specificity of MRI have been the focus of this work.

MRS provides the ability to study various metabolites simply by adjusting our scanning parameters (echo time etc.) to fit metabolites of interest which makes it an attractive and relatively simple tool to use with a lot to be gained from it. Further studies and an increased understanding of the various metabolites linked to neuroinflammation may ultimately lead to the validation of certain metabolites as biomarkers for neuroinflammation.

The use of D_2O as a contrast agent for lung imaging, was not fully explored in this work and perhaps it is an area worth developing, however the emergence of hyperpolarized xenon MRI as the main technique for lung imaging using MRI may draw interest away from the potential role of D_2O.

In the coming months, our research group here in Nottingham aims to demonstrate a new biosensor based on paramagnetic relaxation changes in ^{129}Xe, as opposed to changes in its chemical shift which is the most common approach. This sensor is a continuation of initial work carried out by Zamberlan et al [77] . The sensor will consist of CrA cages, linked to a Gd^{3+} ion through a peptide sequence which will be a substrate for a target enzyme. When the Gd^{3+} is attached to the cage, it will depolarize the signal from encapsulated xenon, and because of the fast exchange (alluded to earlier in Chapter 4) there will be significant decrease in the free xenon signal. Cleavage of the peptide linker by a target enzyme, would result in the Gd^{3+} being shifted away from the cage therefore not having a depolarizing effect on caged xenon meaning there will be no reduction in signal of free xenon. This hyperpolarised xenon biosensor will allow monitoring of enzyme activity at µM concentrations.

There are critical steps to be taken in order for this project to work including the synthesis of the sensor by a postdoctoral chemist, and establishing the cell imaging

setup. This cell imaging setup will be based on an existing setup developed by Rose et al [65]. It will consist of two compartments that can each hold RAW 264.7 macrophages (Sigma-Aldrich), to which the sensor and lipopolysaccharide will be added. Hyperpolarized ^{129}Xe will then be delivered to one or both compartments for imaging. Someone will take charge of the design and testing of this imaging setup, which will be completed prior to the sensor being ready.

Xenon biosensor MRI is an exciting field of research. It has developed rapidly in the last decade, both in the number of applications developed and in the improvement of initial techniques. However, much research remains to be done, particularly with validating these biosensors *in vivo* where there appears to be a lack of research currently.

References

1. Strimbu, K. and J.A. Tavel, *What are Biomarkers?* Current opinion in HIV and AIDS, 2010. **5**(6): p. 463-466.
2. Masumoto, A., et al., *Analysis of intramedullary cell density by MRI using the multiple spin-echo technique.* Am J Hematol, 1997. **55**(3): p. 134-8.
3. Alústiza Echeverría, J.M., A. Castiella, and J.I. Emparanza, *Quantification of iron concentration in the liver by MRI.* Insights into Imaging, 2012. **3**(2): p. 173-180.
4. Christen, T., D.S. Bolar, and G. Zaharchuk, *Imaging brain oxygenation with MRI using blood oxygenation approaches: methods, validation, and clinical applications.* AJNR Am J Neuroradiol, 2013. **34**(6): p. 1113-23.
5. Shah, N.J., V. Ermer, and A.M. Oros-Peusquens, *Measuring the absolute water content of the brain using quantitative MRI.* Methods Mol Biol, 2011. **711**: p. 29-64.
6. Jansen, J.F.A., et al., *1H MR Spectroscopy of the Brain: Absolute Quantification of Metabolites.* Radiology, 2006. **240**(2): p. 318-332.
7. Keeler, J., *Understanding NMR Spectroscopy*. 2011: Wiley.
8. Levitt, M.H., *Spin Dynamics: Basics of Nuclear Magnetic Resonance*. 2001: Wiley.
9. McRobbie, D.W., et al., *MRI from Picture to Proton*. 2007: Cambridge University Press.
10. Harris Robin, K., et al., *NMR nomenclature. Nuclear spin properties and conventions for chemical shifts(IUPAC Recommendations 2001)*, in *Pure and Applied Chemistry*. 2001. p. 1795.
11. Heerschap, A., et al., *In vivo magnetic resonance spectroscopy of transgenic mice with altered expression of guanidinoacetate methyltransferase and creatine kinase isoenzymes.* Subcell Biochem, 2007. **46**: p. 119-48.
12. Braakman, N., et al., *High resolution localized two-dimensional MR spectroscopy in mouse brain in vivo.* Magn Reson Med, 2008. **60**(2): p. 449-56.

13. Blüml, S., *Magnetic Resonance Spectroscopy: Basics*, in *MR Spectroscopy of Pediatric Brain Disorders*, S. Blüml and A. Panigrahy, Editors. 2013, Springer New York: New York, NY. p. 11-23.
14. Streit, W.J., R.E. Mrak, and W.S.T. Griffin, *Microglia and neuroinflammation: a pathological perspective.* Journal of Neuroinflammation, 2004. **1**(1): p. 1-4.
15. Cagnin, A., A. Gerhard, and R.B. Banati, *In vivo imaging of neuroinflammation.* European Neuropsychopharmacology, 2002. **12**(6): p. 581-586.
16. Brand, A., C. Richter-Landsberg, and D. Leibfritz, *Multinuclear NMR studies on the energy metabolism of glial and neuronal cells.* Dev Neurosci, 1993. **15**(3-5): p. 289-98.
17. Miller, B.L., et al., *Alzheimer disease: depiction of increased cerebral myo-inositol with proton MR spectroscopy.* Radiology, 1993. **187**(2): p. 433-7.
18. Castillo, M., J.K. Smith, and L. Kwock, *Correlation of myo-inositol levels and grading of cerebral astrocytomas.* AJNR Am J Neuroradiol, 2000. **21**(9): p. 1645-9.
19. de Graaf, R.A., *In Vivo NMR Spectroscopy: Principles and Techniques*. 2008: Wiley.
20. Blakely, R.D. and J.T. Coyle, *The neurobiology of N-acetylaspartylglutamate.* Int Rev Neurobiol, 1988. **30**: p. 39-100.
21. Taylor, D.L., et al., *Investigation into the role of N-acetylaspartate in cerebral osmoregulation.* J Neurochem, 1995. **65**(1): p. 275-81.
22. Schneider, P., et al., *Central metabolite changes and activation of microglia after peripheral interleukin-2 challenge.* Brain Behav Immun, 2012. **26**(2): p. 277-83.
23. Geurts, J.J., et al., *MR spectroscopic evidence for thalamic and hippocampal, but not cortical, damage in multiple sclerosis.* Magn Reson Med, 2006. **55**(3): p. 478-83.
24. Gideon, P., et al., *Early time course of N-acetylaspartate, creatine and phosphocreatine, and compounds containing choline in the brain after acute stroke. A proton magnetic resonance spectroscopy study.* Stroke, 1992. **23**(11): p. 1566-72.

25. Erecinska, M. and I.A. Silver, *Metabolism and role of glutamate in mammalian brain.* Prog Neurobiol, 1990. **35**(4): p. 245-96.
26. Lehnardt, S., et al., *The toll-like receptor TLR4 is necessary for lipopolysaccharide-induced oligodendrocyte injury in the CNS.* J Neurosci, 2002. **22**(7): p. 2478-86.
27. Venneti, S., C.A. Wiley, and J. Kofler, *Imaging microglial activation during neuroinflammation and Alzheimer's disease.* J Neuroimmune Pharmacol, 2009. **4**(2): p. 227-43.
28. Lim, S.L., C.J. Rodriguez-Ortiz, and M. Kitazawa, *Infection, systemic inflammation, and Alzheimer's disease.* Microbes and Infection, 2015. **17**(8): p. 549-556.
29. Devanand, D.P., et al., *Hippocampal and entorhinal atrophy in mild cognitive impairment: prediction of Alzheimer disease.* Neurology, 2007. **68**(11): p. 828-36.
30. Du, A.T., et al., *Magnetic resonance imaging of the entorhinal cortex and hippocampus in mild cognitive impairment and Alzheimer's disease.* J Neurol Neurosurg Psychiatry, 2001. **71**(4): p. 441-7.
31. Provencher, S.W., *Estimation of metabolite concentrations from localized in vivo proton NMR spectra.* Magn Reson Med, 1993. **30**(6): p. 672-9.
32. Hennig, J., A. Nauerth, and H. Friedburg, *RARE imaging: a fast imaging method for clinical MR.* Magn Reson Med, 1986. **3**(6): p. 823-33.
33. Gruetter, R., *Automatic, localized in vivo adjustment of all first- and second-order shim coils.* Magn Reson Med, 1993. **29**(6): p. 804-11.
34. Perry, V.H. and C. Holmes, *Microglial priming in neurodegenerative disease.* Nat Rev Neurol, 2014. **10**(4): p. 217-224.
35. Boretius, S., et al., *Halogenated volatile anesthetics alter brain metabolism as revealed by proton magnetic resonance spectroscopy of mice in vivo.* Neuroimage, 2013. **69**: p. 244-55.
36. Wang, F.N., et al., *Water signal attenuation by D2O infusion as a novel contrast mechanism for 1H perfusion MRI.* NMR Biomed, 2013. **26**(6): p. 692-8.

37. Spence, M.M., et al., *Functionalized xenon as a biosensor.* Proceedings of the National Academy of Sciences, 2001. **98**(19): p. 10654-10657.
38. Schroder, L., et al., *Molecular imaging using a targeted magnetic resonance hyperpolarized biosensor.* Science, 2006. **314**(5798): p. 446-9.
39. Paul Preuss. (2002). *Building a better biosensor: xenon in a cage.*Available: http://www2.lbl.gov/Science-Articles/Archive/MSD-PBD-xenon-biosensor.html. Last accessed 8th November 2016.
40. Riggle, B.A., Y. Wang, and I.J. Dmochowski, *A "Smart" 129Xe NMR Biosensor for pH-Dependent Cell Labeling.* Journal of the American Chemical Society, 2015. **137**(16): p. 5542-5548.
41. Wei, Q., et al., *Designing 129Xe NMR biosensors for matrix metalloproteinase detection.* J Am Chem Soc, 2006. **128**(40): p. 13274-83.
42. Zhang, J., et al., *Rational design of hyperpolarized xenon NMR molecular sensor for the selective and sensitive determination of zinc ions.* Talanta, 2014. **122**: p. 101-5.
43. Tassali, N., et al., *Smart Detection of Toxic Metal Ions, Pb2+ and Cd2+, Using a 129Xe NMR-Based Sensor.* Analytical Chemistry, 2014. **86**(3): p. 1783-1788.
44. Miller K. W., et al.,*Xenon NMR: chemical shifts of a general anesthetic in common solvents, proteins, and membranes*. Proc. Natl. Acad. Sci. U. S. A. 1981, 78, 4946–494910.1073/pnas.78.8.4946.
45. Oros, A.M. and N.J. Shah, *Hyperpolarized xenon in NMR and MRI.* Phys Med Biol, 2004. **49**(20): p. R105-53.
46. Albert, M.S., et al., *Biological magnetic resonance imaging using laser-polarized 129Xe.* Nature, 1994. **370**(6486): p. 199-201.
47. Woodhouse, N., et al., *Combined helium-3/proton magnetic resonance imaging measurement of ventilated lung volumes in smokers compared to never-smokers.* J Magn Reson Imaging, 2005. **21**(4): p. 365-9.
48. Lilburn, D.M.L., et al., *Investigating lung responses with functional hyperpolarized xenon-129 MRI in an ex vivo rat model of asthma.* Magnetic Resonance in Medicine, 2015: p. n/a-n/a.

49. Lilburn, D.M.L., G.E. Pavlovskaya, and T. Meersmann, *Perspectives of hyperpolarized noble gas MRI beyond 3He.* Journal of Magnetic Resonance, 2013. **229**: p. 173-186.

50. Imai, H., et al., *Effect of reduced pressure on the polarization of 129Xe in the production of hyperpolarized 129Xe gas: Development of a simple continuous flow mode hyperpolarizing system working at pressures as low as 0.15 atm.* Concepts in Magnetic Resonance Part B: Magnetic Resonance Engineering, 2008. **33B**(3): p. 192-200.

51. Six, J.S., et al., *Pathway to cryogen free production of hyperpolarized Krypton-83 and Xenon-129.* PLoS One, 2012. **7**(11): p. e49927.

52. Goodson, B.M., *Nuclear magnetic resonance of laser-polarized noble gases in molecules, materials, and organisms.* J Magn Reson, 2002. **155**(2): p. 157-216.

53. Ward, K.M., A.H. Aletras, and R.S. Balaban, *A new class of contrast agents for MRI based on proton chemical exchange dependent saturation transfer (CEST).* J Magn Reson, 2000. **143**(1): p. 79-87.

54. Goffeney, N., et al., *Sensitive NMR detection of cationic-polymer-based gene delivery systems using saturation transfer via proton exchange.* J Am Chem Soc, 2001. **123**(35): p. 8628-9.

55. McConnell, H.M., *Reaction Rates by Nuclear Magnetic Resonance.* The Journal of Chemical Physics, 1958. **28**(3): p. 430-431.

56. Finbloom, J.A., et al., *Rotaxane-mediated suppression and activation of cucurbit[6]uril for molecular detection by (129)Xe hyperCEST NMR.* Chem Commun (Camb), 2016. **52**(15): p. 3119-22.

57. Schnurr, M., et al., *Supramolecular Assays for Mapping Enzyme Activity by Displacement-Triggered Change in Hyperpolarized (129)Xe Magnetization Transfer NMR Spectroscopy.* Angew Chem Int Ed Engl, 2015. **54**(45): p. 13444-7.

58. Shapiro, M.G., et al., *Genetically encoded reporters for hyperpolarized xenon magnetic resonance imaging.* Nat Chem, 2014. **6**(7): p. 629-634.

59. Roukala, J., et al., *Encapsulation of xenon by a self-assembled Fe4L6 metallosupramolecular cage.* J Am Chem Soc, 2015. **137**(7): p. 2464-7.

60. Guo, Q., et al., *A Molecular Imaging Approach to Mercury Sensing Based on Hyperpolarized (129)Xe Molecular Clamp Probe.* Chemistry, 2016. **22**(12): p. 3967-70.

61. Jeong, K., et al., *Investigation of DOTA–Metal Chelation Effects on the Chemical Shift of 129Xe.* ChemPhysChem, 2015. **16**(17): p. 3573-3577.

62. Khan, N.S., et al., *Cryptophane-folate biosensor for (129)xe NMR.* Bioconjug Chem, 2015. **26**(1): p. 101-9.

63. Klippel, S., C. Freund, and L. Schroder, *Multichannel MRI labeling of mammalian cells by switchable nanocarriers for hyperpolarized xenon.* Nano Lett, 2014. **14**(10): p. 5721-6.

64. Korchak, S., W. Kilian, and L. Mitschang, *Degeneracy in cryptophane-xenon complex formation in aqueous solution.* Chem Commun (Camb), 2015. **51**(9): p. 1721-4.

65. Korchak, S., et al., *Design and comparison of exchange spectroscopy approaches to cryptophane-xenon host-guest kinetics.* J Magn Reson, 2016. **265**: p. 139-45.

66. Kotera, N., et al., *A doubly responsive probe for the detection of Cys4-tagged proteins.* Chem Commun (Camb), 2015. **51**(57): p. 11482-4.

67. Rose, H.M., et al., *Development of an antibody-based, modular biosensor for 129Xe NMR molecular imaging of cells at nanomolar concentrations.* Proc Natl Acad Sci U S A, 2014. **111**(32): p. 11697-702.

68. Rossella, F., et al., *Design and Characterization of Two Bifunctional Cryptophane A-Based Host Molecules for Xenon Magnetic Resonance Imaging Applications.* ChemPlusChem, 2014. **79**(10): p. 1463-1471.

69. Schnurr, M., et al., *Brain endothelial cell targeting via a peptide-functionalized liposomal carrier for xenon hyper-CEST MRI.* Adv Healthc Mater, 2015. **4**(1): p. 40-5.

70. Schnurr, M., C. Witte, and L. Schroder, *Depolarization Laplace transform analysis of exchangeable hyperpolarized (1)(2)(9)Xe for detecting ordering phases and cholesterol content of biomembrane models.* Biophys J, 2014. **106**(6): p. 1301-8.

71. Taratula, O., et al., *Enantiopure Cryptophane-129Xe Nuclear Magnetic Resonance Biosensors Targeting Carbonic Anhydrase.* Supramol Chem, 2015. **27**(1-2): p. 65-71.

72. Tyagi, R., et al., *Dendronized cryptophanes as water-soluble xenon hosts for (129)Xe magnetic resonance imaging.* Org Lett, 2014. **16**(17): p. 4436-9.

73. Witte, C., et al., *Live-cell MRI with xenon hyper-CEST biosensors targeted to metabolically labeled cell-surface glycans.* Angew Chem Int Ed Engl, 2015. **54**(9): p. 2806-10.

74. Berthault, P., et al., *Sensitivity and multiplexing capabilities of MRI based on polarized 129Xe biosensors.* J Am Chem Soc, 2008. **130**(49): p. 16456-7.

75. Schroder, L., *Xenon for NMR biosensing--inert but alert.* Phys Med, 2013. **29**(1): p. 3-16.

76. Darzac, M., et al. (2004). *Synthesis and application of cryptophanol hosts: 129Xe NMR spectroscopy of a deuterium-labeled (Xe)2@bis-cryptophane complex*. *New Journal of Chemistry*. 28 (4), 502-512.

77. Zamberlan, F., Lesbats, C., Rogers, N. J., Krupa, J. L., Pavlovskaya, G. E., Thomas, N. R., Faas, H. M. and Meersmann, T. (2015), *Molecular Sensing with Hyperpolarized ^{129}Xe Using Switchable Chemical Exchange Relaxation Transfer.* ChemPhysChem, 16: 2294–2298. doi:10.1002/cphc.201500367